



VRIJE
UNIVERSITEIT
BRUSSEL

¹ **A search for flavour changing neutral currents
2 involving a top quark and a Z boson, using the
3 data collected by the CMS collaboration at a
4 centre of mass of 13 TeV**

⁵ Van Parijs, Isis

⁶ Proefschrift ingediend met het oog op het behalen van de academische graad
⁷ Doctor in de Wetenschappen.

Published in Faculteit Wetenschappen & Bio-ingenieurswetenschappen
Vrije Universiteit Brussel
At 1. June 2017.

⁸

Responsible Contact: I. Van Parijs
Institute for High Energy Physics
Promotor: Prof. Jorgen D'Hondt

9 First Referee: Prof. Dr. J. D'Hondt
 Date of Hand-in: 10 November 2017
 Date of Defense: 10 December 2017

Contents

| | | |
|----|---|----|
| 11 | 1 An introduction to the theory | 1 |
| 12 | 1.1 Elementary particles and forces | 1 |
| 13 | 1.2 Standard Model Lagrangian | 3 |
| 14 | 1.3 Flavour changing currents in the SM | 5 |
| 15 | 1.4 Motivations for new physics | 6 |
| 16 | 1.5 An effective approach beyond the SM: FCNC involving a top quark | 8 |
| 17 | 1.6 Experimental constraints on top-FCNC | 10 |
| 18 | 2 Experimental set-up | 13 |
| 19 | 2.1 The Large Hadron Collider | 13 |
| 20 | 2.1.1 LHC design and operation | 15 |
| 21 | 2.2 The Compact Muon Solenoid | 17 |
| 22 | 2.2.1 CMS coordinate system | 18 |
| 23 | 2.2.2 Towards the heart of CMS | 19 |
| 24 | 2.2.3 Data acquisition | 28 |
| 25 | 2.2.4 CMS computing model | 28 |
| 26 | 3 Analysis techniques | 31 |
| 27 | 3.1 Event generation | 31 |
| 28 | 3.1.1 Fundamentals of simulating a proton collision | 31 |
| 29 | 3.1.2 Programs for event generation | 32 |
| 30 | 3.1.3 Generating FCNC top-Z interactions | 33 |
| 31 | 3.1.4 Generating background events | 35 |
| 32 | 3.2 Multivariate analysis techniques: Boosted Decision Trees | 35 |
| 33 | 3.3 Template-based fitting | 35 |
| 34 | Bibliography | 37 |

Theoretical basis

1

36 The Standard Model (SM) [1] is a name given in 1970s to a theory describing the fundamental
 37 particles and their interactions. This quantum field theory describes the particles and their
 38 interactions as fields and has successfully incorporated three of the four fundamental forces in
 39 the universe. In [Section 1.1](#), the particle content of the SM is summarised, while [Section 1.2](#)
 40 describes the SM Lagrangian and its symmetries. In [Section 1.3](#), the flavour content of the SM
 41 is highlighted. The successful theory of the SM has some shortcomings which are discussed
 42 in [Section 1.4](#) and lead to searches for a more general theory. One of such a search is using
 43 effective field theory (EFT). In [Section 1.5](#) an EFT model focussing on flavour changing neutral
 44 currents (FCNC) involving a top quark is presented. Its current experimental constraints are
 45 given in [Section 1.6](#).

46 The physics search presented in this thesis relies on statistical tools and interpretations. In
 47 [Section ??](#), the notion of a likelihood is presented as well as maximum likelihood fits. To set
 48 upper limits on a signal process the confidence levels method is used. The background modelling
 49 is checked using goodness-of-fit tests. Furthermore, the search will use multivariate analysis
 50 methods which are also explained.

51 1.1 Elementary particles and forces

52 The interactions in nature can be described by four forces, the strong force, the electromagnetic
 53 (EM) force, the weak force and the gravitational force. These interactions happen via particles
 54 with an integer spin known as bosons. The strong interaction is mediated by eight gluons g ,
 55 while the electromagnetic force is mediated by photons γ , and the weak force by Z and W^\pm
 56 bosons. In [Table 1.1](#), the forces and their characteristics are shown. The gravitational force is
 57 the only force not included in the SM and can be neglected for energies lower than the Planck
 58 scale ($1.22 \cdot 10^{19}$ GeV).

59 The fermions are the particles that make up the visible matter in the universe. They carry half
 60 integer spin and can be subdivided into leptons and quarks, where leptons don't interact strongly.
 61 Each fermion has a corresponding anti-fermion which has the same mass and is oppositely
 62 charged. The electron e^- is the first elementary particle discovered [2] and belongs to the first
 63 generation of leptons together with electron neutrino ν_e . The second generation is made up

Table 1.1: The four forces of nature and their characteristics.

| | Range | Mediator |
|-----------------------|---------------|--------------------|
| Strong force | $10^e - 15$ m | 8 gluons |
| Electromagnetic force | ∞ | photon |
| Weak force | 10^{-18} m | W^\pm , Z bosons |
| Gravitational force | ∞ | unknown |

64 of the muon μ^- and the muon neutrino ν_μ , whereas the third generation consists of the tau
 65 τ and the tau neutrino ν_τ . The neutrino's are neutral particles, while the other leptons have
 66 charge $\pm q_e$ where q_e represents the elementary charge of $1.602 \cdot 10^{-19}$ C. The masses of the
 67 charged leptons differ by four orders of magnitude between the first and third generations. In
 68 the SM the neutrino's are assumed to be massless, while it is experimentally established that
 69 neutrino do have a tiny non-zero mass. In [Table 1.2](#), the leptons and their properties in the SM
 are summarised.

Table 1.2: The properties of the leptons in the three generations of the SM [3], where q_e represents the elementary charge.

| Generation | Particle | Mass | Charge |
|------------|------------|-------------|--------|
| First | e^- | 0.511 MeV | $-q_e$ |
| | ν_e | ≈ 0 | 0 |
| Second | μ^- | 106 MeV | $-q_e$ |
| | ν_μ | ≈ 0 | 0 |
| Third | τ | 1 777 MeV | $-q_e$ |
| | ν_τ | ≈ 0 | 0 |

70

71 The quarks can also be divided into three generations. Unlike the leptons, they carry colour
 72 charge and can interact via the strong interaction. The top quark, discovered in 1995 at the
 73 Tevatron [4, 5] is the heaviest SM particle with a mass close to 173.1 ± 0.6 GeV¹ [3]. The quarks
 74 and their properties are summarized in [Table 1.3](#). In nature, only colour neutral objects can exist.
 75 This has as consequence that quarks are bound through gluons into mesons (quark+anti-quark)
 76 and baryons (three quarks). These mesons and baryons are mostly short-lived and unstable
 77 particle that rapidly decay through W^\pm and Z bosons, associated with a fermion. The only
 78 known stable baryon is the proton, made up of two up quarks and one down quark.

79 The scalar boson, commonly known as the Higgs boson, is the last piece of the SM and is
 80 discovered in 2012 [6, 7]. It is responsible for the masses of the W^\pm and Z boson, and that of
 81 the fermions.

¹In this thesis all masses and energies are expressed in natural units, where the speed of light and \hbar are taken to be equal to one.

Table 1.3: The properties of the quarks in the three generations of the SM [3], where q_e represents the elementary charge.

| | Generation | Particle | Mass | Charge |
|--------|------------|----------------------------|--------------------|--------|
| First | up u | $2.2^{+0.6}_{-0.4}$ MeV | $\frac{2}{3} q_e$ | |
| | down d | $4.7^{+0.5}_{-0.4}$ MeV | $\frac{-1}{3} q_e$ | |
| Second | charm c | 1.28 ± 0.03 GeV | $\frac{2}{3} q_e$ | |
| | strange s | 96^{+8}_{-4} MeV | $\frac{-1}{3} q_e$ | |
| Third | top t | 173.1 ± 0.6 GeV | $\frac{2}{3} q_e$ | |
| | bottom b | $4.18^{+0.04}_{-0.03}$ GeV | $\frac{-1}{3} q_e$ | |

82 1.2 Standard Model Lagrangian

83 The SM is a quantum field theory and thus describes the dynamics and kinematics of particles
 84 and forces by a Lagrangian \mathcal{L} . The theory is based on the $SU_C(3) \times SU_L(2) \times U_Y(1)$ gauge
 85 symmetry, where $SU_L(2) \times U_Y(1)$ describes the electroweak interaction and $SU_C(3)$ the strong
 86 coupling. The indices refer to colour C, the left chiral nature of the $SU_L(2)$ coupling L, and the
 87 weak hypercharge Y. Its Lagrangian is constructed such that contains symmetries representing
 88 physics conservation laws such as conservation of energy, momentum and angular momentum.
 89 By imposing gauge invariance the symmetries under local group transformations are sustained.

The $U_Y(1)$ group has one generator Y with an associated gauge field B_μ . The three gauge fields W_μ^1 , W_μ^2 , and W_μ^3 , are associated to $SU_L(2)$ with three generators that can be written as half of the Pauli matrices:

$$T_1 = \frac{1}{2} \begin{pmatrix} 0 & 1 \\ 1 & 0 \end{pmatrix}, T_2 = \frac{1}{2} \begin{pmatrix} 0 & -i \\ i & 0 \end{pmatrix}, \text{ and } T_3 = \frac{1}{2} \begin{pmatrix} 1 & 0 \\ 0 & -1 \end{pmatrix}. \quad (1.1)$$

The generators T^a satisfy the Lie algebra:

$$[T^a, T^b] = i\epsilon^{abc} T_c \text{ and } [T^a, Y] = 0, \quad (1.2)$$

90 where ϵ^{abc} is an antisymmetric tensor. The gauge fields of $SU_L(2)$ only couple to left-handed
 91 fermions as required by the observed parity violating nature of the weak force. The $SU_C(3)$
 92 group represents quantum chromodynamics (QCD). It has eight generators corresponding to
 93 eight gluon fields $G_\mu^{1\dots 8}$. Unlike $SU_L(2) \times U_Y(1)$, $SU_C(3)$ is not chiral.

Under $SU_C(3)$ quarks are colour triplets while leptons are colour singlets. This implies that the quarks carry a colour index ranging between one and three, whereas leptons do not take part in strong interactions. Based on the chirality, the quarks and leptons are organized in doublets or singlets. Each generation i of fermions consists of left-handed doublets and right-handed singlets:

$$l_L = \begin{pmatrix} e^-_L \\ \nu_L \end{pmatrix}, e^-_R, q_L = \begin{pmatrix} u_L \\ d_L \end{pmatrix}, u_R, \text{ and } d_R \quad (1.3)$$

NOTE:
should I explain gauge invariance or is a reference enough?

The SM Lagrangian can be decomposed as a sum of four terms

$$\mathcal{L}_{\text{SM}} = \mathcal{L}_{\text{gauge}} + \mathcal{L}_f + \mathcal{L}_{\text{Yuk}} + \mathcal{L}_\phi, \quad (1.4)$$

that are related to the gauge, fermion, Yukawa and scalar sectors. The gauge Lagrangian regroups the gauge fields of all three symmetry groups, and the fermionic part consists of kinetic energy terms for quarks and leptons. The interaction between fermions and the scalar doublet ϕ gives rise to fermion masses and is described by the Yukawa Lagrangian. The scalar part of the Lagrangian is composed of a kinematic and potential component related to the scalar boson.

For the electroweak theory, two coupling constants are introduced, namely g' for $U_Y(1)$ and g for $SU_L(2)$. The physically observable gauge bosons of this theory are the photon field A_μ , the Z boson field Z_μ^0 , and the W field W_μ^\pm . These are a superposition of the four gauge fields of $SU_L(2) \times U_Y(1)$:

$$A_\mu = \sin\theta_W W_\mu^1 + \cos\theta_W B_\mu, \quad Z_\mu^0 = \cos\theta_W W_\mu^3 - \sin\theta_W B_\mu, \quad \text{and} \quad W_\mu^\pm = \sqrt{\frac{1}{2}} (W_\mu^1 \mp W_\mu^2), \quad (1.5)$$

where θ_W represents the weak mixing angle defined as $\tan\theta_W = \frac{g'}{g}$.

The coupling constant representing the strength of the QCD interactions is denoted as g_s . In QCD there is asymptotic freedom whereby the strong coupling constant becomes weaker as the energy with which the interaction between strongly interacting particles is probed increases, and stronger as the distance between the particles increases. A consequence of this is known as colour confinement. The quarks and gluons can not exist on their own and are not observed individually. They are bound in colour neutral states called hadrons, this process is known as hadronisation.

107 Electroweak symmetry breaking

In $\mathcal{L}_{\text{gauge}}$ and \mathcal{L}_f are no mass terms for fermions present because only singlets under $SU_C(3) \times SU_L(2) \times U_Y(1)$ can acquire a mass with an interaction of the type $m^2 \phi^\dagger \phi$ without breaking the gauge invariance. In order to accommodate mass terms for fermions and gauge fields, electroweak symmetry breaking, leading to \mathcal{L}_ϕ is introduced.

The scalar doublet is introduced in the SM as

$$\phi = \frac{1}{\sqrt{2}} \begin{pmatrix} \varphi_1 + i\varphi_2 \\ \varphi_3 + i\varphi_4 \end{pmatrix}. \quad (1.6)$$

NOTE:
check if I
need to add
constants
here

Its field potential is of the form

$$V(\phi) = \mu^2 \phi^\dagger \phi + \lambda (\phi^\dagger \phi)^2, \quad (1.7)$$

with $\mu^2 < 0$ and λ a positive integer. This choice of parameters gives the potential a "Mexican hat" shape. It has an infinite set of minima (ground states) and by expanding the field around an arbitrary choice of ground state, the electroweak symmetry is broken (EW):

$$\phi = \begin{pmatrix} 0 \\ \frac{v}{\sqrt{2}} \end{pmatrix} + \hat{\phi}, \quad (1.8)$$

where v is the vacuum expectation value (vev), measured to be around 245 GeV and corresponds to $\sqrt{\frac{-\mu}{\lambda}}$. The scalar doublet's four degrees of freedom is reduced to three degrees of freedom that couple to the gauge fields and mix with the W^+ , W^- and Z bosons. The remaining fourth degree of freedom has given rise to a physically observable particle, called the Brout-Englert-Higgs (BEH) boson. This spontaneous symmetry breaking leaves the gauge invariance intact and gives masses to the W^\pm and Z bosons as:

$$m_W = \frac{1}{2}v|g| \quad \text{and} \quad m_Z = \frac{1}{2}v\sqrt{g'^2 + g^2}. \quad (1.9)$$

- 112 The Brout-Englert-Higgs field couples universally fermions with a strength proportional to their
 113 masses, and to gauge bosons with a strength proportional to the square of their masses.

114 1.3 Flavour changing currents in the SM

Flavour changing charged currents are introduced in 1963 by Nicola Cabibbo [8]. Via interaction with a W boson the flavour of the quarks is changed. At the time of the postulation, only up, down and strange quarks were known and the charged weak current was described as a coupling between the up quark and d_{weak} , where d_{weak} is a linear combination of the down and strange quarks, $d_{\text{weak}} = \cos\theta_c d + \sin\theta_c s$. This linear combination is a direct consequence of the chosen rotation

$$\begin{pmatrix} d_{\text{weak}} \\ s_{\text{weak}} \end{pmatrix} = \begin{pmatrix} \cos\theta_c & \sin\theta_c \\ -\sin\theta_c & \cos\theta_c \end{pmatrix} \begin{pmatrix} d \\ s \end{pmatrix} = \mathcal{R} \begin{pmatrix} d \\ s \end{pmatrix}, \quad (1.10)$$

where the rotation angle θ_c is known as the Cabibbo angle. This provides a definition for the charged weak current between u and d quarks,

$$J_\mu = \bar{u} \gamma_\mu (1 + \gamma_5) d_{\text{weak}}. \quad (1.11)$$

A consequence of Cabibbo's approach is that the s_{weak} is left uncoupled, leading to Glashow, Iliopoulos and Maiani (GIM) [9–11] to require the existence of a fourth quark with charge $\frac{2}{3}$. This quark, known as the charm quark, couples to s_{weak} and a new definition of the charged weak current is modified to

$$J_\mu = (u \ c) \gamma_\mu (1 + \gamma_5) \mathcal{R} \begin{pmatrix} d \\ s \end{pmatrix} = \bar{U} \gamma_\mu (1 + \gamma_5) \mathcal{R} D. \quad (1.12)$$

The neutral weak current is defined as

$$J_3 = \bar{U} \gamma_\mu (1 + \gamma_5) [\mathcal{R}, \mathcal{R}^\dagger] D, \quad (1.13)$$

- 115 and is diagonal in flavour space. This has as consequence that no flavour changing neutral
 116 currents occur at tree-level Feynmann diagrams².

²Feynmann diagrams are physical representation of interaction between particles. They are based on Feynmann rules [1].

NOTE:
should I
explain
feynmann
diagrams?

Kobayashi and Maskawa generalised the Cabibbo rotation matrix to accommodate for a third generation of quarks. The result is a 3×3 unitary matrix known as the CKM matrix, responsible for the mixing of weak interaction states of down-type quarks:

$$\begin{pmatrix} d_{\text{weak}} \\ s_{\text{weak}} \\ b_{\text{weak}} \end{pmatrix} = \begin{pmatrix} V_{ud} & V_{us} & V_{ub} \\ V_{cd} & V_{cs} & V_{cb} \\ V_{td} & V_{ts} & V_{tb} \end{pmatrix} \begin{pmatrix} d \\ s \\ b \end{pmatrix} = \mathcal{V}_{\text{CKM}} \begin{pmatrix} d \\ s \\ b \end{pmatrix}. \quad (1.14)$$

The unitarity of the matrix ($\mathcal{V}_{\text{CKM}}^\dagger \mathcal{V}_{\text{CKM}} = \mathbb{1}$). A general 3×3 unitary matrix depends on three real angles and six phases. For the CKM matrix, the freedom to redefine the phases of the quark eigenstates can remove five of the phases, leaving a single physical phase known as the Kobayashi-Maskawa phase. This phase is responsible for the charge parity violation in the SM [12]. Each element V_{ij} of \mathcal{V}_{CKM} represents the transition probability of a quark i going to a quark j , and is experimentally determined to be [3]

$$\mathcal{V}_{\text{CKM}} = \begin{pmatrix} 0.97425 \pm 0.00022 & 0.2253 \pm 0.0008 & (4.13 \pm 0.49)10^{-3} \\ 0.225 \pm 0.008 & 0.986 \pm 0.016 & (41.1 \pm 1.3)10^{-3} \\ (8.4 \pm 0.6)10^{-3} & (40.0 \pm 2.7)10^{-3} & 1.021 \pm 0.032 \end{pmatrix}. \quad (1.15)$$

From Equation 1.15 follows that top quarks predominantly decay via charged weak currents to bottom quarks, with a probability consistently with unity. In the SM, FCNC can only occur via higher loop Feynmann diagrams which are highly suppressed. The expected transition probabilities for a top quark decaying via a FCNC interaction in the SM are given in Table 1.4, where it is clear that the FCNC sector of the SM is still beyond the reach of the sensitivity of current experiments.

Table 1.4: The predicted branching ratios \mathcal{B} for FCNC interactions involving the top quark in the SM [13]

| Process | \mathcal{B} in the SM | Process | \mathcal{B} in the SM |
|-------------------------|-------------------------|-------------------------|-------------------------|
| $t \rightarrow uZ$ | $8 \cdot 10^{-17}$ | $t \rightarrow cZ$ | $1 \cdot 10^{-14}$ |
| $t \rightarrow u\gamma$ | $4 \cdot 10^{-16}$ | $t \rightarrow c\gamma$ | $5 \cdot 10^{-14}$ |
| $t \rightarrow ug$ | $4 \cdot 10^{-14}$ | $t \rightarrow cg$ | $5 \cdot 10^{-12}$ |
| $t \rightarrow uH$ | $2 \cdot 10^{-17}$ | $t \rightarrow cH$ | $3 \cdot 10^{-15}$ |

122

1.4 Motivations for new physics

Many high energy experiments confirm the success of the SM. In particular the scalar boson, the cornerstone of the SM, has consecrated the theory. Unfortunately there are also strong indications that the SM ought to be a lower energy expression of a more global theory. The existence of physics beyond the SM(BSM) [14] is strongly motivated. These motivations are based on direct evidence from observation such as the existence of neutrino masses, the existence of dark matter and dark energy, or the matter-antimatter asymmetry, and also from theoretical problems such as the hierarchy problem, the coupling unification or the large numbers of free parameters in the SM.

NOTE: 124
Reread and elaborate 125

126

132 In the SM, the neutrino is assumed to be massless, whilst experiments with solar, atmospheric,
 133 reactor and accelerator neutrinos have established that neutrinos can oscillate and change
 134 flavour during flight [15, 16]. These oscillations are only possible when neutrino's have masses.
 135 The flavour neutrinos (ν_e , ν_μ , ν_τ) are then linear expressions of the fields of at least three mass
 136 eigenstate neutrinos ν_1 , ν_2 , and ν_3 .

137 The ordinary or baryonic matter described by the SM describes only 5% of the mass (energy)
 138 content of the universe. Astrophysical evidence indicated that dark matter is contributing
 139 to approximately 27%, and dark energy to 68% of the content of the universe. From the
 140 measurements of the temperature and polarizations anisotropies of the cosmic microwave
 141 background by the Planck experiment [17], the density of cold non baryonic matter is determined.
 142 Cold dark matter is assumed to be only sensitive to the weak and gravitational force, leading
 143 to only one possible SM candidate: the neutrino. However, these are too light to account for
 144 the vast amount of dark matter and other models are needed. Dark energy is assumed to be
 145 responsible for the acceleration in the expansion of the universe [18].

146 At the big bang matter and antimatter is assumed to be produced in equal quantities. However,
 147 it is clear that we are surrounded by matter. So where did all the antimatter go? In 1967,
 148 Sakharov identified three mechanisms that are necessary to obtain a global matter antimatter
 149 asymmetry [19]. These mechanisms are baryon and lepton number violation, at a given moment
 150 in time there was a thermal imbalance for the interactions in the universe, and there is charge
 151 C and charge parity CP violation³. The large numbers of free parameters in the SM are taken
 152 as nine fermion masses, three CKM mixing angles and one CP violating phase, one EM coupling
 153 constant g' , one weak coupling constant g , one strong coupling constant g_s , one QCD vacuum
 154 angle, one vacuum expectation value, and one mass of the scalar boson. This large number of
 155 free parameters lead to the expectation of a more elegant, general theory beyond the SM.

156 The hierarchy problem [20] is related to the huge difference in energy between the weak
 157 scale and the Planck scale. The vev of the Brout-Englert-Higgs field determines the weak scale
 158 that is approximately 246 GeV. The radiative corrections to the scalar boson squared mass m_H^2 ,
 159 coming from its self couplings and couplings to fermions and gauge bosons, are quadratically
 160 proportional to the ultraviolet momentum cut-off Λ_{UV} . This cut-off is at least equal to the energy
 161 to which the SM is valid without the need of new physics. The SM is valid up to the Planck mass
 162 making the correction to m_H^2 about thirty orders of magnitude larger than m_H^2 . This implies that
 163 an extraordinary cancellation of terms should happen. This is also known as the naturalness
 164 problem of the H boson mass.

The correction to the squared mass of the scalar boson coming from a fermion f , coupling to
 the scalar field ϕ with a coupling λ_f is given by

$$\Delta m_H^2 = -\frac{|\lambda_f|^2}{8\pi^2} \Lambda_{UV}^2, \quad (1.16)$$

³The rate of a process $i \rightarrow f$ can be different from the CP-conjugate process: $\tilde{i} \rightarrow \tilde{f}$. The SM includes sources of CP-violation through the residual phase of the CKM matrix. However, these could not account for the magnitude of the asymmetry observed.

while the correction to the mass from a scalar particle S with a mass m_S , coupling to the scalar field with a Lagrangian term $-\lambda_{\text{mathrm}{S}}|\phi|^2|S|^2$ is

$$\Delta m_H^2 = -\frac{|\lambda_S|^2}{16\pi^2} \left(\Lambda_{\text{UV}}^2 - 2m_S^2 \ln\left(\frac{\Lambda_{\text{UV}}}{m_S}\right) + \dots \right). \quad (1.17)$$

As one can see the correction term to m_H^2 is much larger than m_H^2 itself. By introducing BSM physic models that introduce new scalar particles at TeV scale that couple to the scalar boson can cancels the Λ_{UV}^2 divergence and avoid this fine-tuning.

Also the large mass differences between the fermions related to the Yukawa couplings can go up to six order of magnitude in the case of the electron and the top quark and constitute the fermion mass hierarchy problem.

The choice of the $SU_C(3) \times SU_L(2) \times U_Y(1)$ symmetry group itself as well as the separate treatment of the three forces included in the SM raises concern. The intensity of the forces show a large disparity around the electroweak scale, but have comparable strengths at higher energies. The electromagnetic and weak forces are unified in a electroweak interaction, but the strong coupling constant does not encounter the other coupling constants at high energies. In order to reach a grand unification, the running of couplings can be modified by the addition of new particles in BSM models.

1.5 An effective approach beyond the SM: FCNC involving a top quark

The closeness of the top mass to the electroweak scale led physicist to believe that it is a sensitive probe for new physics. Its property study is therefore an important topic of the experimental program at the LHC. Several extensions of the SM enhance the FCNC branching ratios and can be probed at the LHC [13], from which some of them are shown in Table 1.5. Previous searches have been performed at the Fermilab Tevatron by the CDF [21] and D0 [22] collaborations, and at the LHC by the ATLAS [23–26] and CMS [27–31] collaborations.

NOTE:
check
with refer-
ences from
TOP2017

Table 1.5: The predicted branching ratios \mathcal{B} for FCNC interactions involving the top quark in some BSM models [13]: quark singlet (QS), generic two Higgs doublet model (2HDM) and the minimal super symmetric extensions to the SM (MSSM);

| Process | QS | 2HDM | MSSM | Process | QS | 2HDM | MSSM |
|-------------------------|--------------------------|--------------------------|------------------------|-------------------------|--------------------------|----------------|------------------------|
| $t \rightarrow uZ$ | $\leq 1.1 \cdot 10^{-4}$ | — | $\leq 2 \cdot 10^{-6}$ | $t \rightarrow cZ$ | $\leq 1.1 \cdot 10^{-4}$ | $\leq 10^{-7}$ | $\leq 2 \cdot 10^{-6}$ |
| $t \rightarrow u\gamma$ | $\leq 7.5 \cdot 10^{-9}$ | — | $\leq 2 \cdot 10^{-6}$ | $t \rightarrow c\gamma$ | $\leq 7.5 \cdot 10^{-9}$ | $\leq 10^{-6}$ | $\leq 2 \cdot 10^{-6}$ |
| $t \rightarrow ug$ | $\leq 1.5 \cdot 10^{-7}$ | — | $\leq 8 \cdot 10^{-5}$ | $t \rightarrow cg$ | $\leq 1.5 \cdot 10^{-7}$ | $\leq 10^{-4}$ | $\leq 8 \cdot 10^{-5}$ |
| $t \rightarrow uH$ | $\leq 4.1 \cdot 10^{-5}$ | $\leq 5.5 \cdot 10^{-6}$ | $\leq 10^{-5}$ | $t \rightarrow cH$ | $\leq 4.1 \cdot 10^{-5}$ | $\leq 10^{-3}$ | $\leq 10^{-5}$ |

185

The impact of BSM models can written in a model independent way by means of an effective field theory valid up to an energy scale Λ . The leading effects are parametrized by a set of

188 fully gauge symmetric dimension-6 operators that are added to the SM Lagrangian and can be
 189 reduced to a minimal set of operators as discussed in [32, 33]. The full Lagrangian, neglecting
 190 neutrino physics, in the fully gauge symmetric case is given by

$$\mathcal{L}_{\text{SM+EFT}} = \mathcal{L}_{\text{SM}} + \sum_i \frac{\bar{c}_i}{\Lambda^2} \mathcal{O}_i + \mathcal{O}\left(\frac{1}{\Lambda^3}\right), \quad (1.18)$$

where the Wilson coefficients \bar{c}_i depend on the considered theory and on the way that new physics couples to the SM particles. Considering that Λ is large, contributions suppressed by powers of Λ greater than two are neglected. Moreover, all four fermion operators are omitted for the rest of this thesis. After electroweak symmetry breaking the operators induce [13, 34] both corrections to the SM couplings and new interactions at tree level such as FCNC interactions. The FCNC interactions of the top quark that are not present in the SM are given by

$$\mathcal{L}_{\text{EFT}}^t = \frac{\sqrt{2}}{2} \sum_{q=u,c} \left[g' \frac{\kappa_{t\gamma q}}{\Lambda} A_{\mu\nu} \bar{t} \sigma^{\mu\nu} (f_{\gamma q}^L P_L + f_{\gamma q}^R P_R) q \right. \quad (1.19)$$

$$+ \frac{g}{2\cos\theta_W} \frac{\kappa_{tZq}}{\Lambda} Z_{\mu\nu} \bar{t} \sigma^{\mu\nu} (f_{Zq}^L P_L + f_{Zq}^R P_R) q \quad (1.20)$$

$$+ \frac{\sqrt{2}}{4\cos\theta_W} \zeta_{tZq} \bar{t} \gamma^\mu (\tilde{f}_q^L P_L + \tilde{f}_q^R P_R) q Z_\mu \quad (1.21)$$

$$+ g_S \frac{\kappa_{gqt}}{\Lambda} Z_{\mu\nu} \bar{t} \sigma^{\mu\nu} (f_{gq}^L P_L + f_{gq}^R P_R) q G_\mu^a \quad (1.22)$$

$$+ \eta_{Hqt} \bar{t} (\hat{f}_q^L P_L + \hat{f}_q^R P_R) q H + \text{h.c.} \Big], \quad (1.23)$$

where the value of the FCNC couplings at scale Λ are represented by $\kappa_{tZq}, \kappa_{gqt}, \kappa_{t\gamma q}, \zeta_{tZq}$, and η_{Hqt} . These are assumed to be real and positive, with the unit of GeV^{-1} for κ_{txq}/Λ and no unit for ζ_{xqt} and η_{xqt} . In the equation $\sigma^{\mu\nu}$ equals to $\frac{i}{2} [\gamma^\mu, \gamma^\nu]$, and the left- and right-handed chirality projector operators are denoted by P_L and P_R . The electromagnetic coupling constant is denoted by g' , the strong interaction coupling is denoted as g_s , while the electroweak interaction is parametrised by the coupling constant g and the electroweak mixing angle θ_W . The complex chiral parameters are normalized according to $|f_{xq}^L|^2 + |f_{xq}^R|^2 = 1$, $|\tilde{f}_q^L|^2 + |\tilde{f}_q^R|^2 = 1$, and $|\hat{f}_q^L|^2 + |\hat{f}_q^R|^2 = 1$. In the expression for $\mathcal{L}_{\text{EFT}}^t$, the unitary gauge is adopted on the scalar field is expanded around its vacuum expectation value with H being the SM scalar boson, and the field strength tensors of the photon A_μ , the gluon field $G_\mu^{1..8}$, and the Z boson Z_μ^0 are defined as

$$A_{\mu\nu} = \partial_\mu A_\nu - \partial_\nu A_\mu, Z_{\mu\nu} = \partial_\mu Z_\nu - \partial_\nu Z_\mu, \text{ and } G_{\mu\nu} = \partial_\mu G_\nu^a - \partial_\nu G_\mu^a + g_S f_{bc}^a G_\mu^b G_\nu^c. \quad (1.24)$$

191 Denoting the structure constant of the $SU_C(3)$ group as f_{bc}^a . Note that there are two coupling
 192 constants arising in $\mathcal{L}_{\text{EFT}}^t$, which is a residue of electroweak symmetry breaking. The massive Z
 193 boson will appear in both the Z_μ^0 field as well as the covariant derivative, leading to an extra
 194 Z-vertex.

¹⁹⁵ **1.6 Experimental constraints on top-FCNC**

Experiments commonly put limits on the branching ratio's which allow an easier interpretation across different EFT models as

$$\mathcal{B}(t \rightarrow qX) = \frac{\delta_{txq}^2 \Gamma_{t \rightarrow qX}}{\Gamma_t}, \quad (1.25)$$

¹⁹⁶ where $\Gamma_{t \rightarrow qX}$ represents the FCNC decay width⁴ for a coupling strength $\delta_{txq}^2 = 1$, and Γ_t the full
¹⁹⁷ decay width of the top quark. In the SM, supposing a top quark mass of 172.5 GeV, the full
¹⁹⁸ width becomes $\Gamma_t^{\text{SM}} = 1.32$ GeV [35].

¹⁹⁹ Searches for top-FCNC usually adopt a search strategy depending on the experimental set-up
²⁰⁰ and the FCNC interaction of interest, looking either for FCNC interactions in the production of
²⁰¹ a single top quark or in its decay for top pair interactions. In Figure 1.1, these two cases are
²⁰² shown for the tZq vertex.

²⁰³

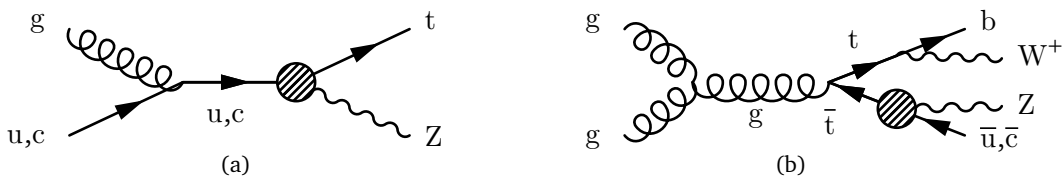


Figure 1.1: Feynman diagrams for the tZq FCNC interaction, where the FCNC interaction is indicated with the shaded dot. (a) Single top production through an FCNC interaction. (b) Top pair production with an FCNC induced decay.

²⁰⁴ The observation of top-FCNC interactions has yet to come and experiments have so far only
²⁰⁵ been able to put upper bounds on the branching ratios. An overview of the best current limits is
²⁰⁶ given in Table 1.6. In Figure 1.2 a comparison is shown between the current best limits set by
²⁰⁷ ATLAS and CMS with respect to several BSM model benchmark predictions. From there one can
²⁰⁸ see that FCNC searches involving a Z or H boson are close to excluding or confirming several
²⁰⁹ BSM theories.

NOTE: Check at-las result for tZq from top2017 proceedings when they appear

⁴The decay width of a certain process represents the probability per unit time that a particle will decay. The total decay width, defined as all possible decay widths of a particle, is inversely proportional to its lifetime.

Table 1.6: Overview of the most stringent observed and expected experimental limits on top-FCNC branching ratios \mathcal{B} at 95% confidence level.

| Process | Search mode | Observed \mathcal{B} | Expected \mathcal{B} | Experiment |
|-------------------------|--|------------------------|------------------------|------------|
| $t \rightarrow uZ$ | top pair decay and single top production | $2.2 \cdot 10^{-4}$ | $2.7 \cdot 10^{-4}$ | CMS [27] |
| $t \rightarrow u\gamma$ | single top production | $1.3 \cdot 10^{-4}$ | $1.9 \cdot 10^{-4}$ | CMS [29] |
| $t \rightarrow ug$ | single top production | $4.0 \cdot 10^{-5}$ | $3.5 \cdot 10^{-5}$ | ATLAS [24] |
| $t \rightarrow uH$ | top pair decay | $2.4 \cdot 10^{-3}$ | $1.7 \cdot 10^{-3}$ | ATLAS [26] |
| $t \rightarrow cZ$ | top pair decay and single top production | $4.9 \cdot 10^{-4}$ | $12 \cdot 10^{-4}$ | CMS [27] |
| $t \rightarrow c\gamma$ | single top production | $2.0 \cdot 10^{-3}$ | $1.7 \cdot 10^{-3}$ | CMS [29] |
| $t \rightarrow cg$ | single top production | $2.0 \cdot 10^{-4}$ | $1.8 \cdot 10^{-4}$ | ATLAS [24] |
| $t \rightarrow cH$ | top pair decay | $2.2 \cdot 10^{-3}$ | $1.6 \cdot 10^{-3}$ | CMS [26] |

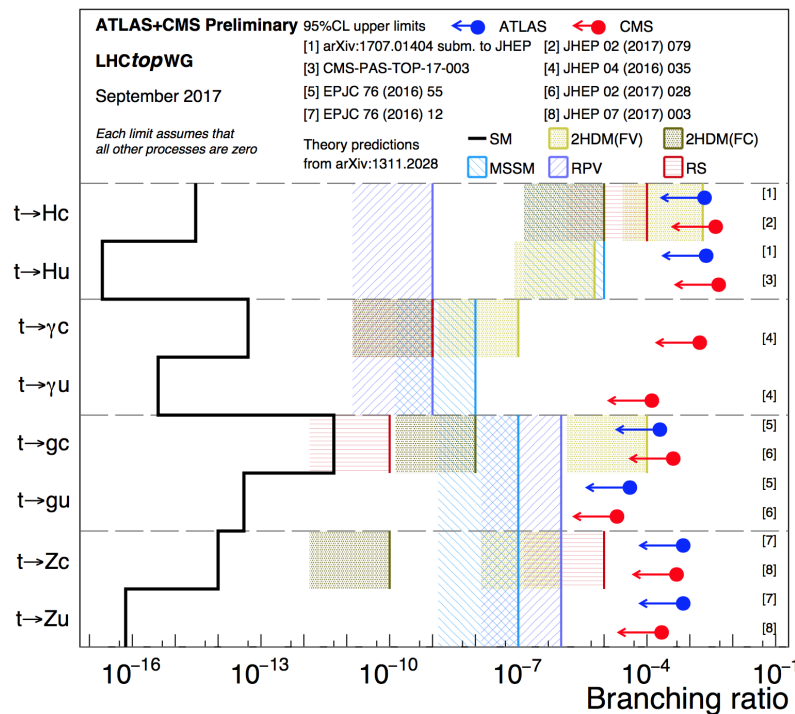


Figure 1.2: Current best limits set by CMS and ATLAS for top-FCNC interactions.

Experimental set-up

2

211 The main objective of the Large Hadron Collider (LHC) was the search for the Brout-Englert-
 212 Higgs boson (or scalar boson). It was known from the Linear Electron Positron(LEP)[36] and
 213 Tevatron[37] experiments that the scalar boson mass had to be larger than 114 GeV[38, 39],
 214 and smaller than around 1 TeV due to unitarity and perturbativity constraints [40]. On top of
 215 this, the search of supersymmetry or dark matter were part of the motivation for building the
 216 LHC. Since the start of its operation, the LHC is pushing the boundaries of the Standard Model,
 217 putting the best limits on physics beyond the Standard Model as well as precision measurements
 218 of the parameters of the Standard Model. One such an accomplishment is the discovery the
 219 scalar boson in 2012 by the two largest experiments at the LHC [6, 7].

220 In the first part of this chapter, the LHC and the acceleration process for protons to reach
 221 their design energies is discussed. The second part presents the Compact Muon Solenoid.

222 2.1 The Large Hadron Collider

223 The LHC has started its era of cutting edge science on 10 September 2008 [41] after approval by
 224 the European Organisation of Nuclear Research (CERN) in 1995 [42]. Installed in the previous
 225 Large Electron Positron collider (LEP) tunnels, the LHC consists of a 26.7 km ring, that is
 226 installed between 45 and 170 m under the French-Swiss border between Cessy (France) and
 227 Meyrin (Switzerland). Built to study rare physics phenomena at high energies, the LHC has the
 228 possibility to accelerate two type of particles - protons or ions Pb^{45+} - and provides collisions
 229 at four points of interaction or bunch crossings.. At the interaction points, experiments are
 230 installed in order to study the collisions.

231 As can be seen in [Figure 2.1](#), the LHC is last element in a chain of creation, injection and
 232 acceleration of protons. Protons are obtained by ionising hydrogen and injected in a linear
 233 accelerator (LINAC 2), where they obtain an energy of 50 MeV. They continue to the proton
 234 synchrotron booster (PSB or Booster), where the proton packets are accelerated to 1.4 GeV and
 235 are split up in twelve. The proton synchrotron (PS) increases their energy to 25 GeV before
 236 handing the protons to the super proton synchrotron (SPS), where the proton reach an energy
 237 of 450 GeV. Each accelerator ring increases in radius in order to reduce the energy loss of the
 238 protons by synchrotron radiation. This energy loss is proportional to the fourth power of the

239 proton energy and inversely proportional to the bending radius. The protons are then injected
 240 into opposite directions into the LHC, where they are accelerated to 3.5 TeV (in 2010 and
 241 2011), 4 TeV (in 2012 and 2013) or 6.5 TeV (in 2015 and 2016) [43]. Before the start up of
 242 the LHC in 2010, the previous energy record was held by the Tevatron collider at Fermilab,
 243 colliding proton with antiprotons at $\sqrt{s} = 1.96$ TeV.

244 The beam has a bunch structure obtained by the injection scheme and properties of the dump
 245 system. These bunches are obtained in the PS with 25 ns spacing for run II. The operation of
 246 accelerating and transferring to the LHC is repeated 12 times for each counter-rotating beam.
 247 When completely filled, the LHC nominally contains 2220 bunches in run II, compared to 1380
 248 in run I (design: 2200). At full intensity, it would have nearly 2800 bunches but this is limited
 249 due to SPS.

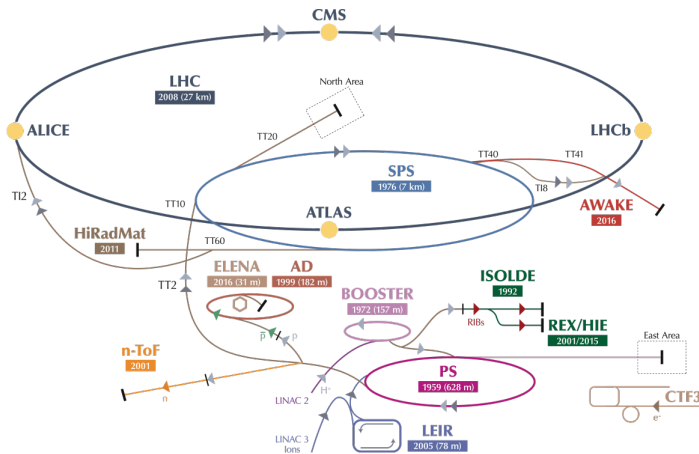


Figure 2.1: Schematic representation of the accelerator complex at CERN [44]. The LHC (dark blue) is the last element in chain of accelerators. Protons are successively accelerated by LINAC 2, the Booster, the Proton Synchrotron (PS) and the Super Proton Synchrotron (SPS) before entering the LHC.

250 The LHC is home to seven experiments that are placed on an interaction point:

- 251 • A Toroidal LHC ApparatuS (ATLAS [45]) and the Compact Muon Solenoid (CMS [46])
 252 experiments are the two general purpose detectors at the LHC. They both have a hermetic,
 253 cylindrical structure and were designed to search for new physics phenomena as well as
 254 precision measurements of the Standard Model. The existence of two distinct experiments
 255 allows cross-confirmation for any discovery.
- 256 • A Large Ion Collider Experiment (ALICE [47]) and the LHC Beauty (LHCb [48]) experiments
 257 are focusing on specific phenomena. ALICE studies strongly interacting matter at extreme
 258 energy densities where quark-gluon plasma forms from heavy ions (Pb-Pb or p-Pb). LHCb
 259 searches for differences between matter and anti matter by means of the b quark, while focussing on CP symmetry violation.
- 260 • The forward LHC (LHCf [49]) and the TOTal cross section, Elastic scattering and diffraction
 261 dissociation Measurement (TOTEM [50]) experiments are two smaller experiments that

263 focus on interactions where protons or heavy ions only meet while head on collisions take
 264 place. LHCf consists of two parts placed before and after ATLAS and studies particles
 265 created at very small angles. TOTEM is placed in the same cavern as CMS and performs
 266 precise measurements of the LHC luminosity.

- 267 • The Monopoles and Exotics Detector At the LHC (MoEDAL [51]) experiment is situated
 268 near LHCb and tries to find magnetic monopoles.

269 **2.1.1 LHC design and operation**

The most important quantity at the LHC is the luminosity[52]. This is a measurement of the number of collisions that can be produced in a detector per m^2 and per second. The LHC collisions create a number of events per second given by

$$N_{\text{event}} = L\sigma_{\text{event}}, \quad (2.1)$$

where σ_{event} is the cross section of the event of interest and L the machine luminosity. This luminosity depends only on the beam parameters and is for a Gaussian beam expressed as

$$L = \frac{1}{4\pi} \textcolor{blue}{N_b} n_b f_{\text{rev}} \frac{\textcolor{red}{N_b}}{\epsilon_n} \left(1 + \left(\frac{\theta_c \sigma_z}{2\sigma^*} \right)^2 \right)^{-\frac{1}{2}} \frac{\gamma_r}{\beta^*}. \quad (2.2)$$

270 The number of particles per bunch is expressed by N_b , while n_b is the number of bunches
 271 per beam, f_{rev} the revolution frequency, γ_r the relativistic gamma factor, ϵ_n the normalized
 272 transverse beam emittance - a quality for the confinement of the beam , β^* the beta function at
 273 the collision point - a measurement for the width of the beam, θ_c the angle between the two
 274 beams at the interaction point, σ_z the mean lengths of one packet, and σ^* the mean height of
 275 one packet. In Equation 2.2), the blue part represents the stream of particles, the red represents
 276 the brilliance; and the green part represents the geometric reduction factor due to the crossing
 277 angle at the interaction point. Hence, in order to enhance the chances for exploration of rare
 278 events and thus enhancing the number of collisions. High beam energies as well as high beam
 279 intensities are required.

280 The peak design luminosity for the LHC in 2016 was $10^{34} \text{ 1}/(\text{m}^2 \text{ s})$, which leads to about 1
 281 billion proton interactions per second. In 2016, the LHC was around 10% above this design
 282 luminosity[53]. This luminosity is not a constant in time. It diminishes due to collisions between
 283 the beams, and the interaction of the protons and the particle gas that is trapped in the centre
 284 of the vacuum tubes due to the magnetic field. The intern diffusion of the beam degrades the
 285 emittance and therefore also the luminosity. For this reason, the mean lifetime of a beam inside
 286 the LHC is around 15 h. The integrated luminosity - the luminosity provided for a certain time
 287 range - recorded by CMS and ATLAS over the year 2016 is given in Figure 2.1.1. In Run II, the
 288 peak luminosity is $13\text{-}17 \cdot 10^{33} \text{ 1}/(\text{cm}^2 \text{ s})$ compared to $7.7 \cdot 10^{33} \text{ 1}/(\text{cm}^2 \text{ s})$ in Run I.

289 Inside the LHC ring [54], the protons are accelerated by the means of radio frequency cavities,
 290 while 1232 magnets of approximately 15 m long, weighing 35 t ensure the deflection of the
 291 beams. The cross section view of such a dipole is given in Figure 2.4. The two proton beams
 292 circulate in opposite direction in separate pipes inside of the magnet. Through the use of a strong

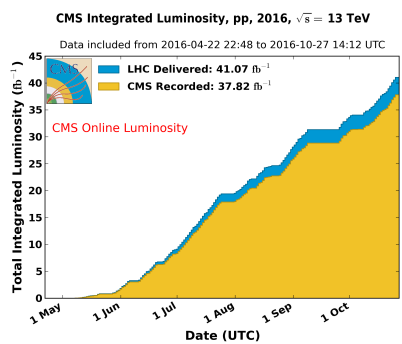


Figure 2.2: Cumulative luminosity measured online versus day delivered to (blue), and recorded by CMS (orange) during stable beams and for proton collisions at 13 TeV centre-of-mass energy in 2016. The delivered luminosity accounts for the luminosity delivered from the start of stable beams until the LHC requests CMS to turn off the sensitive detectors to allow a beam dump or beam studies.

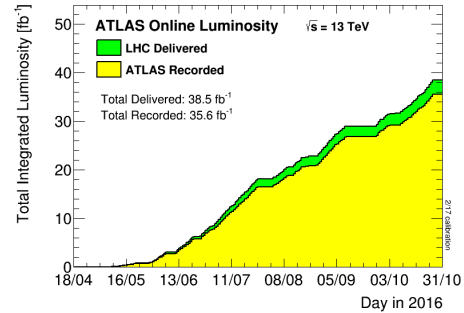


Figure 2.3: Total Integrated Luminosity in 2016 Cumulative luminosity versus time delivered to (green) and recorded by ATLAS (yellow) during stable beams for proton collisions in 2016. The delivered luminosity accounts for the luminosity delivered from the start of stable beams until the LHC requests ATLAS to put the detector in a safe standby mode to allow for a beam dump or beam studies. Shown is the luminosity as determined from counting rates measured by the luminosity detectors.)

293 electric current in the coils around the beam pipe, magnetic fields are generated and cause the
 294 protons to bend in the required orbits. In order to get the coil to become superconducting and
 295 able to produce - with the aid of an iron return yoke - a strong magnetic field of 8.3 T, the
 296 magnet structure is surrounded by a vessel. This vessel is filled with liquid Helium making it
 297 possible to cool down the magnet to 1.9 K. In order to get more focussed and stabilised proton
 298 beam, other higher-order multipole and corrector magnets are placed along the LHC tunnel.

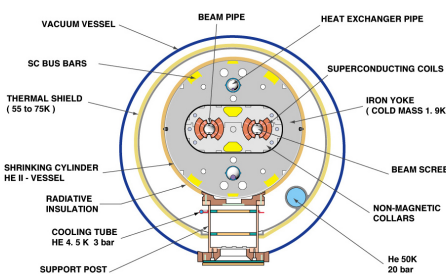


Figure 2.4: Schematic representation of the LHC dipole [55]. Two beam pipes where the proton beams circulate around the LHC ring are shown. The superconducting coils generate a magnetic field of 8.3 T that steer the protons in the circular path.

²⁹⁹ **2.2 The Compact Muon Solenoid**

300 At one of the collision points of the LHC, the CMS detector[56–58] is placed. Weighing 14 000
 301 t, This cylindrical detector is about 28.7 m long and 15 m in diameter, weighing around 14 000
 302 t. It has an onion like structure of several specialised detectors and contains a superconducting
 303 solenoid with a magnetic field of 3.8 T. The CMS detector is designed in a way that it can
 304 address the needs of physics coming from the LHC. Living in a hadronic environment, multi-jet
 305 processes produced by the strong interaction are a main source of background for rare physics
 306 processes. Therefore, good identification, momentum resolution, and charge determination of
 307 muon, electrons and photons is one of the main goals of the CMS detector. Further it provides a
 308 good charged particle momentum resolution and reconstruction efficiency in the inner tracker
 309 such that for example jets coming from b quarks or tau particles can be identified. Also the
 310 electromagnetic resolution for an efficient photon and lepton isolation as well as a good hadronic
 311 calorimeter for the missing transverse energy were kept into account while designing CMS. In
 312 [Figure 2.5](#), an overview of the CMS detector is given.

313 The LHC provides many collisions in a short amount of time. In order to discriminate between
 314 consecutive collisions - known as out of time pile up events - , CMS has to complete the full data
 315 acquisition for one collision event before the next one happens (around 25 ns in Run II and
 316 around 50 ns in Run I [59]). Furthermore, since the photons are in packets, around 21 in Run
 317 I and approximately 40 in Run II inelastic collisions happen every beam crossing . This creates
 318 a great amount of background processes in the detector called in time pile up events. Due to
 319 this difficult conditions, the detector has a high granularity which on its turn creates a need for
 320 huge number of synchronized electronic channels. Furthermore, due to to high flux of particles
 321 in the regions close to the beam, the electronics have to be able to endure high radiation.

322 Before the start of taking collision data for 13 TeV operations on 3 June, CMS had a long
 323 shutdown (LS1)[61]. During this shut down several upgrades were performed. The innermost
 324 part of detection material in CMS (pixel) is made of three concentric cylindrical layers in
 325 run I. At the end of 2016 it is upgraded by adding a fourth layer, enhancing the particle
 326 tracking capabilities of CMS. In order to be able to incorporate this new layer, the section
 327 of the beryllium beam pipe within CMS was replaced by a narrower one during LS1. For
 328 this, the pixel was removed and reinserted into CMS. In order to avoid long damage caused
 329 by the intense particle flux at the heart of CMS, the tracker is been made ready to operate
 330 at much lower temperature than before. During Run I, a small problem was detected in the
 331 electromagnetic calorimeter preshower system. For this, the preshower discs were removed,
 332 repaired and reinstalled successfully inside CMS in 2014. To help the discrimination between
 333 interesting low momentum muons coming from collisions and muons caused by backgrounds, a
 334 fourth triggering and measurement station for muons was added in each of the end caps. CMS
 335 measures the collision rate within the detector and monitors beam related backgrounds. For
 336 this, several new detectors were installed into CMS during LS1.

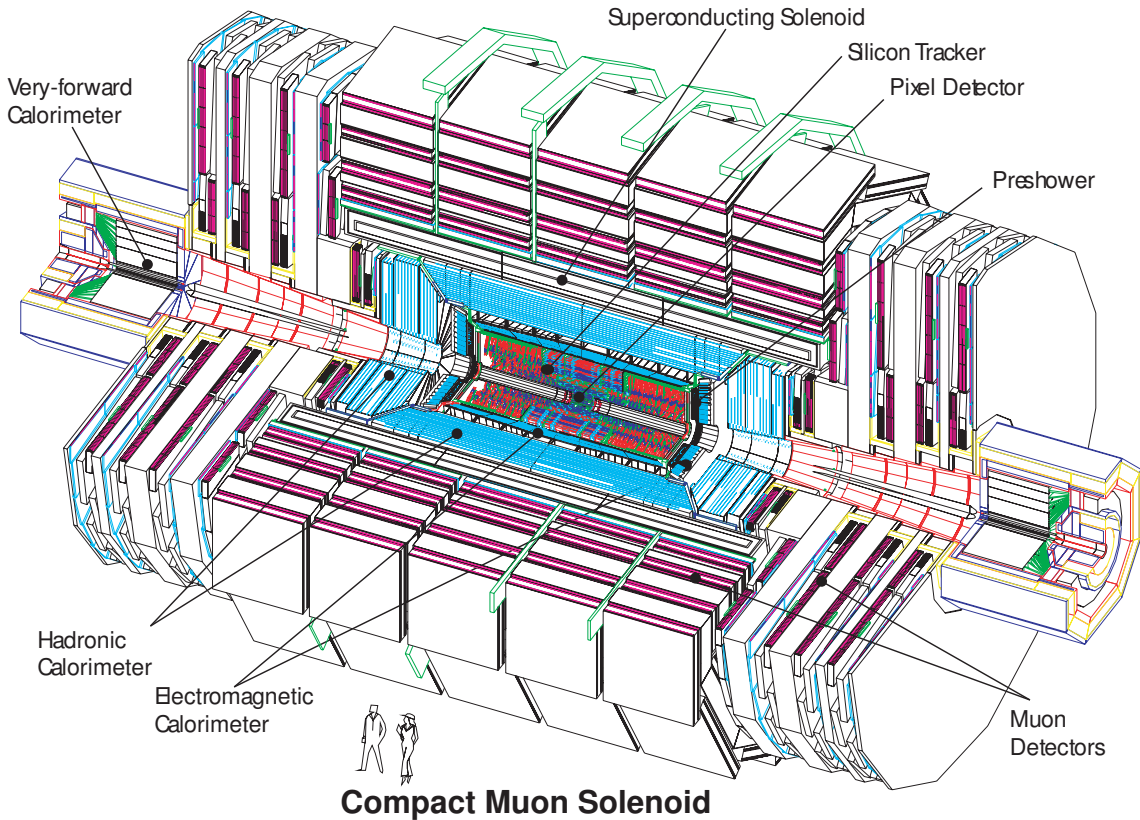


Figure 2.5: Mechanical layout of the CMS detector[60].

337 2.2.1 CMS coordinate system

The coordinate system used by CMS can be found in [Figure 2.6](#). The origin of the right handed orthogonal coordinate system is chosen to be the point of collisions. The x-axis points towards the centre of the LHC ring such that the y-axis points towards the sky, and the z-axis lies tangent to the beam axis. Since the experiment has a cylindrical shape, customary coordinates are used to describe the momentum \vec{p} : the distance ρ , the azimuthal angle $\phi \in [-\pi, \pi]$ - the angle between the x-axis and the projection in the transverse plane of \vec{p} (\vec{p}_T) - , the pseudo-rapidity η - expressed by the polar angle θ between the direction of \vec{p} and the beam - :

$$\eta = -\ln\left(\tan\left(\frac{\theta}{2}\right)\right). \quad (2.3)$$

For the energies considered at the LHC, where $E \gg m$, the pseudo-rapidity is a good approximation of the rapidity y

$$y = \frac{1}{2} \ln\left(\frac{E + p_z}{E - p_z}\right), \quad (2.4)$$

338 where the difference of rapidities of two particles is invariant under a Lorentz boost in the
339 z-direction.

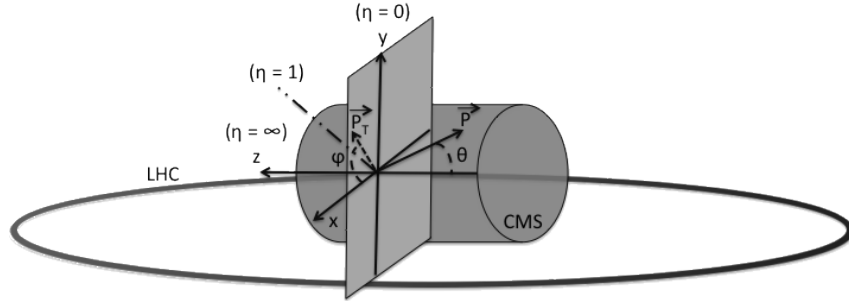


Figure 2.6: Representation of the coordinate system used by CMS. The point of origin is put at the collision point. The x-axis points towards the centre of the LHC ring such that the z-axis lies tangent to the beam axis.

340 2.2.2 Towards the heart of CMS

341 The CMS detector consists of two parts; a central barrel around the beam pipe ($|\eta| < 1.4$) and
 342 two plugs to ensure the hermeticity of the detector. In [Figure 2.5](#) and [Figure 2.7](#) the onion like
 343 structure of the CMS detector is visible. The choice of a solenoid of 12.9 m long and 5.9 m
 344 diameter gives the advantage of bending the particle trajectories in the transverse plane. The
 345 hadronic calorimeter, the electromagnetic calorimeter and the tracker are within the solenoid,
 346 while the muon chambers are placed outside the solenoid.

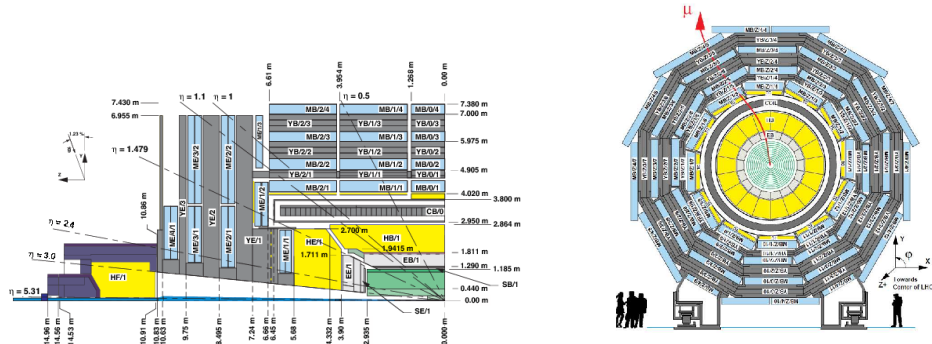


Figure 2.7: Schematic view of the CMS detector in the Run I configuration. (LEFT) Longitudinal view of one quarter of the detector. (RIGHT) Transversal view of one quarter of the detector. The muon system barrel elements are denoted as $MBZ/N/S$, where $z = -2 \dots +2$ is the barrel wheel number, $n = 1 \dots 4$ the station number and $S = 1 \dots 12$ the sector number. Similarly, the steel return yokes are denoted as $YBZ/N/S$. The solenoid is denoted as $CB0$, while the hadronic calorimeter is denoted as HE (end cap)/ HB (barrel)/ HF (forward) and the electromagnetic calorimeter as EE (end cap)/ EB (barrel). The green part represents the tracking system[62]

347 2.2.2.1 Muon system

348 The outermost part of CMS consists of the muon system. The magnet return yoke is interleaved
 349 with gaseous detector chambers for muon identification and momentum measurement. The
 350 barrel contains muon stations arranged in five separate iron wheels, while in the end cap four

351 muon stations are mounted onto three independent iron discs on each side. Each barrel wheel
 352 has 12 sectors in the azimuthal angle.

353 The muon system is divided into three parts, shown in Figure 2.8[62]. The muon rate and
 354 neutron induced backgrounds are small and the magnetic field is very low for the barrel, thus
 355 CMS can use drift tube (DT) chambers. For the end caps however, the muon and background
 356 flux is much higher and there is a need to use cathode strip chambers (CSC) which are able
 357 to provide a faster response, higher granularity and have a better resistance against radiation.
 358 In order to form a redundant trigger system, resistive plate chambers (RPC) are added. This
 359 makes a total of 250 DT chambers, 540 CSC and 610 RPC. In Figure 2.7 the arrangement is
 360 shown.

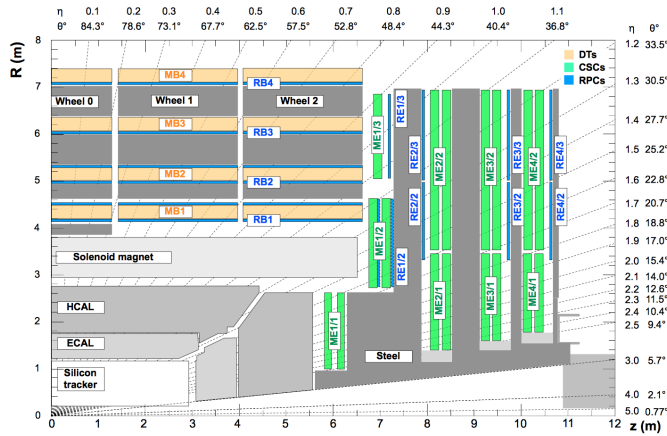


Figure 2.8: Schematic view of one quarter of the CMS muon system in the Run I configuration. [62]

361 Providing a measurement for $|\eta| < 1.2$. The DT chambers in the barrel are on average 2×2.5 m in size and consist of 12 layers of DT cells - 4 cm wide gas tubes with positively
 362 charged stretched wire inside - arranged in three groups of four. The $r\phi$ coordinate is provided
 363 by the two outside groups, while the middle group measures the z coordinate. For each ϕ
 364 sector, the DT chamber is mixed with the flux return yoke. For the outer muon station, the DT
 365 chamber contains only 8 layers of DT cells, providing a muon position in the $r\phi$ plane. There are
 366 four CSC stations in each end cap, providing muon measurements for $0.9 < |\eta| < 2.4$ (Run I
 367 configuration). These CSC are multi-wired proportional chambers that consist of 6 anode wire
 368 planes crossed by 7 copper strips cathode panels in a gas volume. The r coordinate is provided
 369 by the copper strips, while ϕ coordinate comes from the anode wires, giving a two dimensional
 370 position measurement. There are six layers of RPC in the barrel muon system and one layer into
 371 each of the first three stations of the end cap. They are made from two high resistive plastic
 372 plates with an applied voltage and separated by a gas volume. Read out strips mounted on top
 373 of the plastic plates detect the signal generated by a muon passing through the gas volume. The
 374 RPC provides a fast response with a time resolution of 1 ns and covers a range of $|\eta| < 1.8$
 375 (Run I configuration).

377 During the LS1, the muon system underwent major upgrades [63, 64]. In the fourth station
 378 of each end cap, the outermost rings of CSC and RPC chambers were completed, providing an

379 angular region of $1.2 < |\eta| < 1.8$ for Run II, increasing the system redundancy, and allowing
 380 tighter cuts on the trigger quality. In order to reduce the environmental noise, outer yoke discs
 381 have been placed on both sides for the end caps. At the innermost rings of the first station, the
 382 CSC has been upgraded by refurbishing the readout electronics to make use of the full detector
 383 granularity instead of groups of three (Run I).

384 The muon system provides triggering on muons, identifying muons and improves the momentum
 385 measurement and charge determination of high p_T muons. On top of the muon system,
 386 the muon energy is deposited in the electromagnetic calorimeter, the hadronic calorimeter, and
 387 outer calorimeter. The high magnetic field enables an efficient first level trigger and allows a
 388 good momentum resolution of $\Delta p/p \approx 1\%$ for a p_T of 100 GeV and $\approx 10\%$ for a p_T of 1 TeV
 389 (FIXME). There is an efficient muon measurement up to $|\eta| < 2.4$.

390 Muon reconstruction

391 The muon reconstruction[65] has three subdivision: local reconstruction, regional reconstruction
 392 and global reconstruction. The local reconstruction is performed on individual detector elements
 393 such as strip and pixel hits in the inner tracking system, and muon hits and/or segments
 394 on the muon chambers. Independent tracks are reconstructed in the inner tracker - called
 395 tracker track - and in the muon system, called standalone tracks. Based on these tracks,
 396 two reconstructions are considered. The outside-in approach is referred to as Global Muon
 397 reconstruction. For each standalone track, a tracker track is found by comparing the parameters
 398 of the two tracks propagated onto a common surface. Combining the hits from the tracker
 399 track and the standalone track, gives a fit via the Kalman filter technique [66, 67] for a global
 400 muon track. The second approach is an inside-out reconstruction, creating tracker muons. All
 401 candidate tracker tracks are extrapolated to the muon system taking into account the magnetic
 402 field, the average expected energy losses, and multiple Coulomb scattering in the detector
 403 material. When at least one muon segment - DT or CSC hits - matches the extrapolated track,
 404 the corresponding tracker track is indicated as a tracker muon.

405 For low transverse momenta ($p_T \lesssim 5$ GeV), the tracker muon reconstruction is more efficient
 406 than the global muon approach. This is due to the fact that tracker muons only require a
 407 single muon segment in muon system, while the global muon approach requires typically
 408 segments in at least two muon stations. The global muon approach typically improves the
 409 tracker reconstruction for $p_T \gtrsim 200$ GeV.

410 2.2.2.2 Solenoid

411 Making use of the knowledge of previous experiments of ALEPH and DELPHI at LEP and H1
 412 at HERA, CMS choose for a large super conducting solenoid with a length of 12.9 m and
 413 a inner bore of 5.9 m[58]. With 2 168 turns, a current of 19.5 kA and a total energy of 2.7
 414 GJ, a large bending power can be obtained for a modestly-sized solenoid. In order to ensure a
 415 good momentum resolution in the forward regions, a favourable length/radius was necessary.
 416 In [Figure 2.9](#), a photo of the CMS solenoid is given.

417 The solenoid uses a high-purity aluminium stabilised conductor with indirect cooling from
 418 liquid helium, together with fully epoxy impregnation. A four-layer winding is implemented that

419 can withstand an outward pressure of 64 atm. The NbTi cable is co-extruded by pure aluminium
 420 that acts as a thermal stabilizer and has an aluminium alloy for mechanical reinforcement. The
 421 return of the magnetic field is done by five wheels, noted by YB in [Figure 2.7](#).

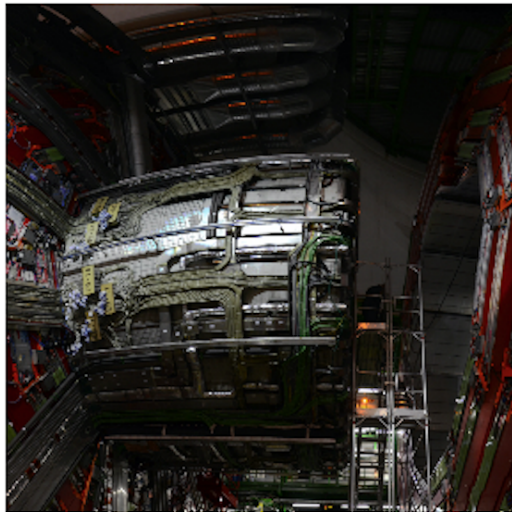


Figure 2.9: CMS solenoid during the long shutdown in 2013.

422 **2.2.2.3 Hadronic calorimeter**

423 The hadronic calorimeter (HCAL) is dedicated to precisely measure the energy of charged and
 424 neutral hadrons via a succession of absorbers and scintillators. This makes it crucial for physics
 425 analyses with hadronic jets or missing transverse energy. The HCAL extends between 1.77
 426 $< r < 2.95$ m where r is the radius in the transverse plane with respect to the beam. Due
 427 to space limitations, the HCAL needs to be as small as possible and is made from materials
 428 with short interaction lengths - the length needed for absorbing 36.7% of the hadrons. The
 429 quality of the energy measurements is dependant on the fraction of the hadronic shower that
 430 can be detected. Therefore, the HCAL barrel (HB) inside the solenoid is reinforced by an outer
 431 hadronic calorimeter between the solenoid and muon detectors (HO, see [Figure 2.10](#)), using the
 432 solenoid as extra absorber. This increases the thickness to 12 interaction lengths. Furthermore,
 433 it should be as hermetic as possible and extend to large pseudo rapidity values. The HB and HO
 434 provide measurements for $|\eta| < 1.3$, while an end cap on each side (HE, $1.3 < |\eta| < 3$) and a
 435 forward calorimeter (HF, $|\eta| < 5.2$) extend the pseudo rapidity range.

436 The HB is made of 16 absorber plates where most of them are built from brass and others
 437 are made from stainless steel and is about five to ten interaction lengths thick. The HE is also
 438 composed of brass absorber plates and has a thickness corresponding to approximately ten
 439 interaction lengths. The HF experiences intense particle fluxes with an energy of 760 GeV
 440 deposited on average in a proton interaction at a center of mass of 14 TeV, compared to 100
 441 GeV in the rest of the detector. Therefore, these are Cherenkov light detectors made of radiation
 442 hard quartz fibers. The main causes of such large energy events are high energy muons, cosmic
 443 particles and charged particles from late showering hadrons. During Run I, it became clear that
 444 the glass windows of the PMTs had to be replaced which was done during LS1 [68]

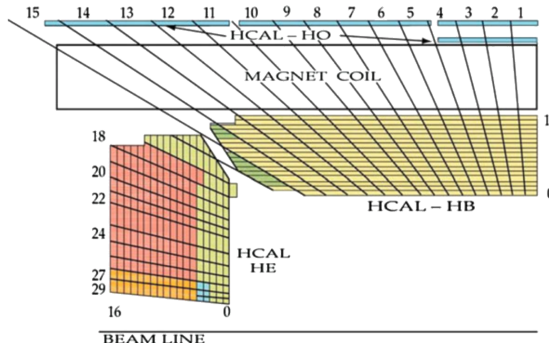


Figure 2.10: Tower segmentation for one quarter of the HCAL displayed in the $r\zeta$ plane[46].

445 2.2.2.4 Electromagnetic calorimeter

446 The electromagnetic calorimeter (ECAL) is designed to measure the energy of photons and
 447 electrons and covers $|\eta| < 3$. It is an hermetic, homogeneous detector and consists of 75 848
 448 lead tungstate (PbWO_4) crystals. These crystals have a fast response time - 80% of the light
 449 is emitted within 25 ns - and are radiation hard. The electromagnetic showers produced by
 450 passing electrons or photons ionize the crystal atoms which emit a blue-green scintillation light,
 451 that is collected by silicon avalanche photodiodes (APDs) in the barrel and vacuum phototriodes
 452 (VPTs) in the end caps. The crystals and the APD response is sensitive to temperature changes
 453 and require a stable temperature.

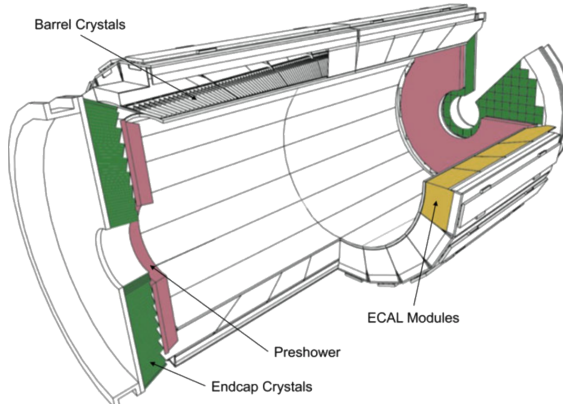


Figure 2.11: Schematic cross section of the electromagnetic calorimeter[46].

454 There are three regions: a central barrel (EB), a endcap region (EE) and a preshower (ES)
 455 (Figure 2.11). The EB has an inner radius of 129 cm and corresponds to a pseudo rapidity
 456 of $0 < |\eta| < 1.479$. At a distance of 314 cm from the vertex and covering a pseudo rapidity
 457 of $1.479 < |\eta| < 3.0$, are the EE. They consist of semi-circular aluminium plates from which
 458 structural units of 5×5 crystals (super crystals) are supported. The ES is placed in front of
 459 the crystal calorimeter over the end cap pseudo rapidity range with two planes of silicon strip
 460 detectors as active elements.

The electromagnetic shower will typically involve more than one channel. More than 90% of

the energy of a 35 GeV electron or photon is contained in a 5×5 matrix of crystals. Therefore, a clustering algorithm is performed in order to associate the energy deposits to the particles impinging the calorimeter. The achieved precision[69] for the barrel is 2.10^{-3} rad in ϕ and 10^{-3} in η . For the end caps this is 5.10^{-3} rad in ϕ and 2.10^{-3} in η . The energy is reconstructed by a super cluster algorithm, taking into account energy radiated via bremsstrahlung or conversion:

$$E_{e/\gamma} = GF_{e/\gamma} \sum_{i \in \text{cluster}} S_i(t) V C_i A_i, \quad (2.5)$$

where G is the absolute energy scale in GeV/ADC, F the energy containment corrections (depends on type of particle, its energy and pseudo rapidity, eg shower leakage and bremsstrahlung losses for electrons), $S(t)$ the relative channel variation with time, C the relative channel response and A the amplitude in ADC counts. The energy resolution is given by

$$\frac{\sigma(E)}{E} = \frac{2.8\%}{\sqrt{E}} \oplus \frac{0.128}{E(\text{GeV})} \oplus 0.3\%, \quad (2.6)$$

461 in the absence of a magnetic field, where the contributions come from the stochastic, noise and
 462 constant terms respectively. The dominating term is the constant term ($E_{\text{shower}} \approx 100\text{GeV}$) and
 463 thus the performance is highly dependent on the quality of calibration and monitoring .

464 In Run I, the energy reconstruction happened via a weighted sum of the digitized samples[70].
 465 For Run II however, the reconstruction had to be made more resistant for out of time pile up
 466 and a multi-fit approach has been set in to place. In this approach, the pulse shape is modelled
 467 as a sum of one in-time pulse plus the out of time pulses [69]. The energy resolution is less
 468 than 2% in the central barrel region and 2-5 % elsewhere.

469 2.2.2.5 Inner tracking system and operations

470 The tracking system (tracker) [71] is the detecting unit closest to the point of interaction.
 471 Responsible for the reconstruction of trajectories from charged particles with $|\eta| < 2.5$ that are
 472 bent by the magnetic field, it provides a measurement of the momentum. The tracker is also
 473 responsible for the determination of the interaction point or vertex. It should be able to provide
 474 high granularity as well as speed, and be able to endure high radiation. For this reason, the
 475 CMS collaboration choose silicon detector technology.

476 The tracking system consists of a cylinder of 5.8 m long and 2.5 m in diameter. It is immersed
 477 in a co-axial magnetic field of 3.8 T due to the solenoid. As shown Figure 2.12, the tracker
 478 is built up from a large silicon strip tracker with a small silicon pixel inside. The inner region,
 479 pixel ($4.4 < r < 10.2$ cm), gets the highest flux of particles. Therefore, pixel silicon sensors
 480 of 100×150 μm area used. It consists of three cylindrical barrels that are complemented by
 481 two discs of pixel modules at each side. The silicon strip tracker ($20 < r < 116$ cm) has three
 482 subdivisions. The Tracker Inner Barrel and Discs (TIB, TID, see Figure 2.14) are composed
 483 of four barrel layers accompanied by three discs at each end. The outer part of the tracker -
 484 Tracker Outer Barrel (TOB) - consists of 6 barrel layers. In the outer discs, there are nine discs
 485 of silicon sensors, referred to as Tracker End Caps (TEC).

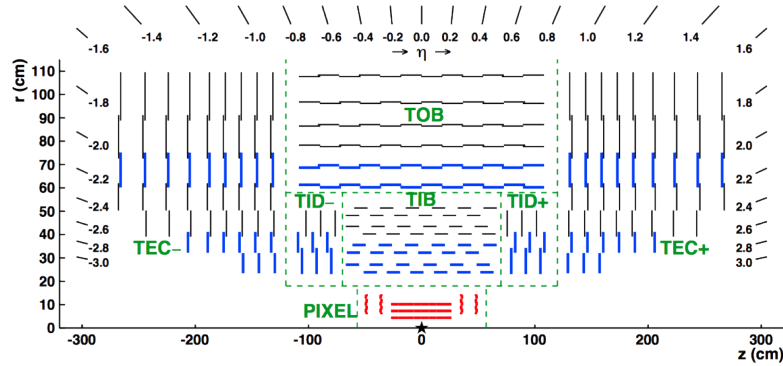


Figure 2.12: Schematic cross section of the top half of the CMS tracking system in the r - z plane. The centre of tracker is shown with a star and corresponds to the approximate position of the proton collision point. The green dashed lines are an indication for each named tracker subsystem. The strip tracker modules that provide two-dimensional hits are shown by thin, black lines, while those able to reconstruct three-dimensional hit positions are shown by thick, blue lines. The pixel modules, shown in red, also provide three-dimensional hits. [57]

486 The pixel, shown in Figure 2.13 has 1440 modules that cover an area of about 1 m² and have
 487 66 million pixels. It provides a three-dimensional position measurement of the hits arising from
 488 the interaction from charged particles with the sensors. In transverse coordinate ($r\phi$), the hit
 489 position resolution is about 10 μm , while 20-40 μm is obtained in the longitudinal coordinate
 490 (z). The sensor plane position provides the third coordinate. The silicon strip trackers consists
 491 of 15 148 single sided modules placed in the TIB, TID and the first four rings of the TEC.
 492 They provide 9.3 million readout channels. In the TOB and the outer three rings of the TEC,
 493 double sided modules are used. These modules are constructed from two back-to-back single
 494 sided modules, where one module is rotated through a stereo angle. This covers an active area
 495 of about 198 m². The TIB and TID provide position measurements in $r\phi$ with a resolution
 496 of approximately 13-38 μm , while the TOB provides a resolution of about 18-47 μm . The
 497 resolution in the z direction is approximately 230 μm in the TIB/TID and 530 μm in the TOB.
 498 To allow overlay and avoid gaps in acceptance, each module is shifted slightly in r or z with
 499 respect to its neighbouring modules within a layer. With this detector lay out, at least nine
 500 points per charged particle trajectory can be measured in an $|\eta|$ range up to 2.4.

During the first data taking period of the LHC (2010 to 2013), the tracker operated at +4°C. With the higher LHC beam intensities from 2015 onwards, the tracker needs to be operated at much lower temperatures. This is due to the fact with intense irradiation, the doping concentration changes, the leakage current increases proportional to the fluence and the charge collection efficiency decreases due to charge trapping. Mostly the leakage current (I) is affected by the temperature change:

$$I \propto T^2 e^{-\frac{E_g}{2kT}}, \quad (2.7)$$

501 where T is the operating temperature, E_g the band gap and k the Boltzmann constant. There is
 502 approximately a factor 15 between the leakage currents at room temperatures and at -10 °C.

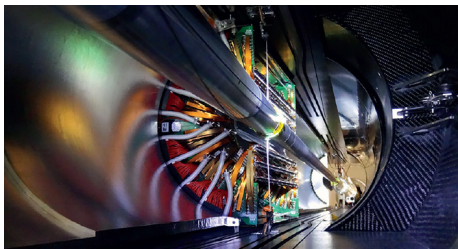


Figure 2.13: The pixel barrel being re-installed after the Long Shutdown in 2015, around the beam pipe at CMS[72]

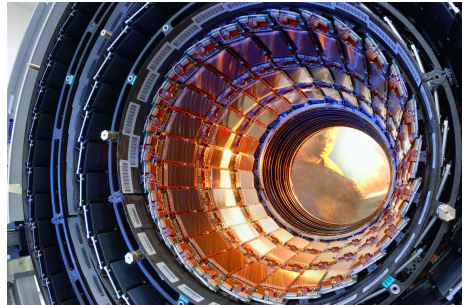


Figure 2.14: First half of the inner tracker barrel, consisting of three layers of silicon modules.[73]

503 During the LS1, the CMS cooling plant was refurbished[74](Figure 2.16) and the fluorocarbon
 504 cooling system overhauled. To help to suppress the humidity inside the tracker, new methods
 505 for vapour sealing and insulation were applied (Figure 2.15). Furthermore, several hundred
 506 high-precision sensors are used to monitor the humidity and temperature. In order to get as
 507 dry air as possible, a new dry-gas plant provides eight times more dry gas (air or nitrogen)
 508 than during the first run, and allows regulation if the flow. As final addition, the cooling
 509 bundles outside the tracker are equipped with heater wires and temperature sensors in order to
 510 maintain safe operations above the cavern dew point For the data taking in 2015-2016, the
 511 tracker operated at -15°C .

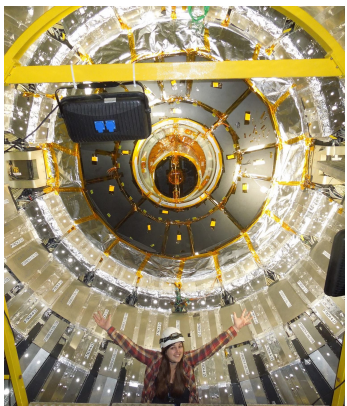


Figure 2.15: Tracker bulkhead being put into closed state with insulation pieces installed during an early trial in fall 2013



Figure 2.16: New Tracker high-capacity dry-gas plant with membrane separation system[61]

512 Track reconstruction

513 An iterative tracking algorithm is responsible for the reconstruction of the tracks made by
 514 charged particles in the inner tracking system. Each iteration consists of four steps[58]: the
 515 track-seed generation, the pattern recognition algorithm, removal of track-hit ambiguities and

516 a final track fit.

517 The seed generation is the first step. It consists of finding reconstructed hits that are usable
 518 for seeding the subsequent track-finding algorithm. They are identified from a group of at
 519 least three reconstructed hits in the tracker, or from a pair of hits while requiring the origin
 520 of the track segment to be compatible with the nominal beam-collision point. Since the pixel
 521 has a higher granularity compared to the strip tracker, its seed generation efficiency is higher.
 522 The overall efficiency exceeds 99%. The second step of each iteration, the pattern recognition
 523 algorithm, uses the seeds as a starting point for a Kalman filter method [66, 67]. This algorithm
 524 extrapolates the seed trajectory towards the next tracker layer taking into account the magnetic
 525 field and multiple scattering effects. The track parameters are updated when a compatible hit
 526 in the next layer is found. This procedure continues until the outermost layer is reached. Since
 527 the Kalman filter method can result in multiple tracks associated to the same seed, or different
 528 tracks sharing the same hits, a removal of ambiguities is necessary. This ambiguity resolving is
 529 done by removing tracks that are sharing too many hits from the list of track candidates. The
 530 tracks with highest number of hits or with the lowest χ^2 if the track fit is kept. The updated
 531 track parameters are then refitted using the Kalman filter method, where all hits found in the
 532 pattern recognition step are taken into account. The fit is done twice - once outwards from the
 533 beam line towards the calorimeters, and inwards from the outermost track hit to the beam line
 534 -, improving the estimation of the track parameters.

535 All hits that are unambiguously associated to the final track are removed from the list of
 536 available hits. In order to associate the remaining hits, the procedure is repeated with looser
 537 track reconstruction criteria. The use of the iterative track reconstruction procedure has a
 538 high track finding efficiency, where the fake track reconstruction rate is negligible. For muons,
 539 this results in a global track reconstruction efficiency exceeding 98%, and 75-98% for charged
 540 hadrons.

541 Primary vertex reconstruction

542 The primary vertex reconstruction should be able to measure the location of all proton interaction
 543 vertices in each event: the signal vertex and all vertices from pile up events. It consists of a vertex
 544 finding and a vertex fitting algorithm and happens in three steps. Tracks are selected to be
 545 consistent with being produced promptly in the primary interaction by imposing requirements
 546 on the track parameters[71] By grouping reconstructed tracks according to the z coordinate of
 547 their closest approach to the beam line, vertices for all interaction in the same beam crossing
 548 are found, at CMS this is done by a deterministic annealing algorithm [75] . On top of this,
 549 a vertex fitting algorithm like the Adaptive Vertex fitter [76], is performed. This creates the
 550 three-dimensional primary-vertex position. With this fit, the contribution from long-lived hadron
 551 decays is reduced by down weighting the tracks with a larger distance to the vertex. The primary
 552 vertex corresponding to the highest sum of squared track transverse momenta is noted as the
 553 point of the main interaction. The resolution on the primary vertex is about 14 μm in $r\phi$ and
 554 about 19 μm in the z direction for primary vertices with the sum of the track $p_T > 100$ GeV
 555 for 2016 data taking.

556 **2.2.3 Data acquisition**

557 At a design luminosity of $10^{34} \text{ 1/(m}^2 \text{ s)}$, the proton interaction rate exceeds 1 GHz. This makes
 558 it impossible for the CMS experiment to store all the data generated. For this, a two level trigger
 559 system has been put in place. The first level (Level-1) is a custom hardware system, while a
 560 second level (HLT) is software based running on a large farm of computers. In run II, with the
 561 increase in centre of mass energy and a higher luminosity, a larger number of simultaneous
 562 inelastic collisions per crossing is expected with respect to run I. For this, the CMS Level-1 has
 563 been upgraded [77].

564 **CMS Level-1 trigger**

565 The Level-1 trigger has to be a flexible, maintainable system, capable of adapting to the evolving
 566 physics programme of CMS [78]. Its output rate is restricted to 100 kHz imposed by the CMS
 567 readout electronics. It is implemented by custom hardware and selects events containing candi-
 568 date objects - eg ionization deposits consistent with a muon, or energy clusters corresponding
 569 to an electron / photon / tau lepton / missing transverse energy / jet. Collisions with large
 570 momenta can be selected by using scalar sum of the transverse momenta of the jets.

571 By buffering the raw data from the CMS subdetectors in front-end drivers, the level-1 trigger
 572 has a pipeline memory of 3.2 μs to decide whether to keep an event or reject it. The trigger
 573 primitives (TP) from the calorimeters and muon detectors are processed in several steps and
 574 combined into a global trigger. This information is then combined with the input from the other
 575 subsystems for the HLT. The separate inputs are synchronized to each other and the LHC orbit
 576 clock and sent to the global trigger module. Here, level-1 trigger algorithms are performed
 577 within 1 μs to decide whether to keep the event.

578 For run II, all hardware, software, databases and the timing control system have been replaced.
 579 The main changes are that the muon system now uses the redundancy of three muon detector
 580 system earlier to make a high resolution muon trigger. Other upgrades are that the calorimeter
 581 system isn't bound any more for streaming data the data and the global trigger has more level-1
 582 trigger algorithms.

583 **CMS HLT trigger**

584 The HLT is an array of commercially available computers with programmable menu that has
 585 output rate of on average 400 Hz for off-line event storage. The data processing is based on a
 586 HLT path. This is a set of algorithmic steps to reconstruct objects and make selections on them.
 587 Here, the information of all sub detectors can be used to perform algorithms on higher level
 588 reconstructed objects.

589 **2.2.4 CMS computing model**

590 The selected data is stored, processed and dispersed via the Worldwide Large Hadron Collider
 591 GRID (WLCG)[79, 80]. This has a tiered structure that function as a single, coherent system:

592 At CERN, a single Tier-0 is located. The raw data collected by CMS is archived here, and
 593 a first reconstruction of the data is done. This data is then already in a file format usable for

594 physics analysis. Furthermore, it is able to reprocess data when new calibrations are made
595 available. The Tier-0 site distributes this data to a total of seven Tier-1 centres. They carry out
596 data reprocessing and store real data as well as simulated data. The Tier-1 further distribute
597 the data to over 50 Tier-2 centres. These make the data accessible for physics analysis and are
598 also being used for the production of simulated data. The data is made accessible for physicists
599 around the world.

Analysis techniques

3

601 3.1 Event generation

602 In order to compare reconstructed data with theoretical predictions, collision events are generated
 603 and passed through a simulation of the CMS detector and an emulation of its readout. For
 604 the detector simulation, a so-called Full Simulation package [81, 82] based on the Geant4
 605 toolkit [83] is employed. It allows a detailed simulation of the interactions of the particles with
 606 the detector material.

607 3.1.1 Fundamentals of simulating a proton collision

608 The procedure of generating $pp \rightarrow X$ events can be subdivided into sequential steps [84–86],
 609 as shown in Figure 3.1.

610 Each proton consists of three valence quarks ($u u d$) and many sea quarks and gluons, called
 611 partons. These partons emerge from each proton within a certain probability density $f(x, Q^2)$,
 612 determined by the momentum fraction x carried by the parton and the momentum transfer
 613 Q^2 . The parton density functions (PDF) [87] give the momentum distribution of the proton
 614 amongst its partons.

615 The interaction of two incoming protons is often soft and elastic leading to events that are not
 616 interesting in the framework of this thesis. More interesting are the hard interaction between
 617 two partons from the incoming protons. The matrix elements (ME) of a hard scattering process
 618 of interest is the starting point of the generation of events. Monte Carlo techniques are used
 619 to sample the corresponding cross section integral and the resulting sample of events reflect
 620 the probability distribution of a process over its final state phase space. After obtaining the
 621 sample of events of the hard interaction, a parton shower (PS) program is used to simulate the
 622 hadronisation of final state partons into hadrons which then can also decay further. Additionally,
 623 radiation of soft gluons or quarks from initial or final state partons is simulated. These are
 624 respectively referred to as initial state radiation (ISR) or final state radiation (FSR). Contributions
 625 from soft secondary interactions, the so-called underlying event (UE), and colour reconnection
 626 effects are also taken into account. A brief overview of the employed programs used for the
 627 event generation of the signal and main background processes used in the search presented in
 628 the thesis are given in Section 3.1.2.

NOTE:
Should I
add more
details?

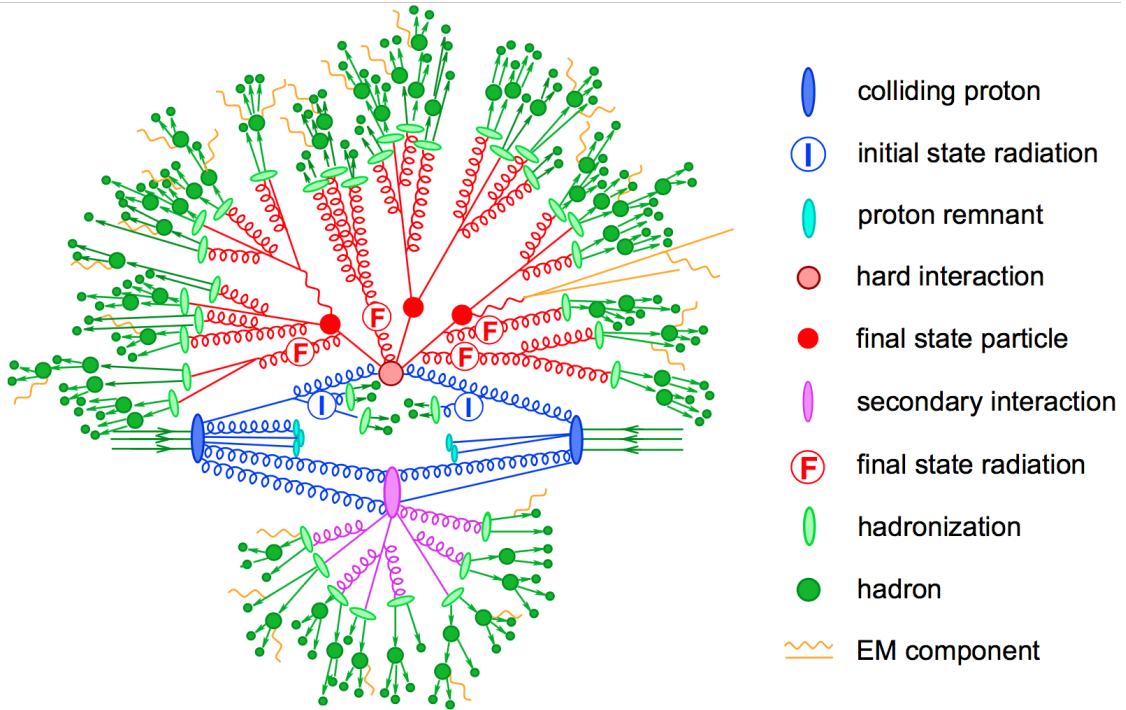


Figure 3.1: Sketch of a hadron collision as simulated by a Monte-Carlo event generator. The red blob in the center represents the hard collision, surrounded by a tree-like structure representing Bremsstrahlung as simulated by parton showers. The purple blob indicates a secondary hard scattering event. Parton-to-hadron transitions are represented by light green blobs, dark green blobs indicate hadron decays, while yellow lines signal soft photon radiation. Figure taken from [86].

629 3.1.2 Programs for event generation

630 The MadGraph5_aMC@NLO program combines the leading order¹ (LO) and the aMC@NLO program
 631 into a common framework. This combination supports the generation of samples at LO or next
 632 to leading order (NLO) together with a dedicated matching to parton showers using the MLM
 633 or MC@NLO schemes respectively. The MC@NLO scheme produces a certain fraction of events
 634 with negative weights originating from the subtraction of amplitudes that contain additional
 635 emissions from the NLO matrix element to prevent double-counting.

636 The POWHEG box (versions 1,2) contains predefined implementations of various processes
 637 at NLO. It applies the POWHEG method for ME- to PS- matching, where the hardest radiation
 638 generated from the ME has priority over subsequent PS emission to remove the overlap with
 639 the PS simulation.

640 The generation of events from processes involving the production and decay of resonances
 641 creates a computational heavy load, especially at NLO. The narrow width approximation the

¹A leading order process is a process which involves the minimal amount of particles. This is also indicated as a tree-level Feynman diagram. Every added interaction vertex increases the order. To obtain the highest precision of an observable quantity the process should consider an infinite amount of orders. Computational limitations limit the process usually the next to leading order.

642 resonant particle is assumed to be on-shell. This makes the production and decay amplitude
 643 factorize, allowing to perform the simulation of the production and decay of heavy resonances
 644 like top quarks or Higgs bosons to be performed in separate steps. The MadSpin program
 645 extends this approach and accounts for off-shell effects through a partial reweighting of the
 646 events. Additionally, spin correlation effects between production and decay products are taken
 647 into account.

648 The Pythia program (versions 6,8) generates events of various processes at LO. Usually in
 649 the analysis, it is however only used for its PS simulation and it is interfaced with other LO and
 650 NLO event generators to perform subsequent parton showering, hadronisation, and simulation
 651 of the underlying event.

652 3.1.3 Generating FCNC top-Z interactions

653 The FCNC processes are generated by interfacing the Lagrangian in [Equation 1.23](#) with
 654 MadGraph5_aMC@NLO by means of the FeynRules package and the Universal FeynRules
 655 Output format. The complex chiral parameters are arbitrary chosen to be $f_{Xq}^L = 0$ and $f_{Xq}^R = 1$.
 656 The signal rates are estimated by use of the MadGraph5_aMC@NLO program for estimating the
 657 partial widths. The anomalous couplings are left free to float for this estimation, and only one
 coupling allowed to be non-vanishing at a time. The results are presented in [Table 3.1](#). The

Table 3.1: Leading order partial widths related to the anomalous decay modes of the top quark, where the new physics scale Λ is given in GeV.

| Anomalous coupling | vertex | Partial decay width (GeV) | |
|------------------------------|--------------|---------------------------|----------------------------------|
| κ_{gqt}/Λ | t g u | $3.665220 \cdot 10^5$ | $(\kappa_{tg_u}/\Lambda)^2$ |
| | t g c | $3.664620 \cdot 10^5$ | $(\kappa_{tg_c}/\Lambda)^2$ |
| $\kappa_{t\gamma q}/\Lambda$ | t γ u | $1.989066 \cdot 10^4$ | $(\kappa_{t\gamma u}/\Lambda)^2$ |
| | t γ c | $1.988904 \cdot 10^4$ | $(\kappa_{t\gamma c}/\Lambda)^2$ |
| κ_{tZq}/Λ | t Z u | $1.637005 \cdot 10^4$ | $(\kappa_{tZu}/\Lambda)^2$ |
| | t Z c | $1.636554 \cdot 10^4$ | $(\kappa_{tZc}/\Lambda)^2$ |
| ζ_{tZq} | t Z u | $1.685134 \cdot 10^{-1}$ | $(\zeta_{tZu})^2$ |
| | t Z c | $1.684904 \cdot 10^{-1}$ | $(\zeta_{tZc})^2$ |
| η_{tHq} | t H u | $1.904399 \cdot 10^{-1}$ | $(\eta_{tHu})^2$ |
| | t H c | $1.904065 \cdot 10^{-1}$ | $(\eta_{tHc})^2$ |

658 anomalous single top cross sections are calculated by convolution of the hard scattering matrix
 659 elements with the LO order set of CTEQ6 partons densities. The NLO effects are modelled by
 660 multiplying each LO cross section by a global k -factor. The LO single top production cross
 661 section and the global k -factors for the top-Z production are shown in [Table 3.2](#). The hard
 662 scattering events are then matched to parton showers to Pythia to account for the simulation of
 663 the QCD environment relevant for hadronic collisions.

Table 3.2: Leading order single top production cross section for $pp \rightarrow tZ$ or $\bar{t} Z$, where the new physics scale is given in GeV. The NLO k -factors are given in the last column.

| Anomalous coupling | Cross section (pb) | NLO k -factor |
|------------------------------|--------------------|----------------------------------|
| κ_{tgu}/Λ | $3.272 \cdot 10^7$ | $(\kappa_{tgu}/\Lambda)^2$ |
| κ_{tgc}/Λ | $3.021 \cdot 10^6$ | $(\kappa_{tgc}/\Lambda)^2$ |
| $\kappa_{t\gamma u}/\Lambda$ | $2.260 \cdot 10^5$ | $(\kappa_{t\gamma u}/\Lambda)^2$ |
| $\kappa_{t\gamma c}/\Lambda$ | $2.654 \cdot 10^4$ | $(\kappa_{t\gamma c}/\Lambda)^2$ |
| κ_{tZu}/Λ | $1.728 \cdot 10^6$ | $(\kappa_{tZu}/\Lambda)^2$ |
| κ_{tZc}/Λ | $2.040 \cdot 10^5$ | $(\kappa_{tZc}/\Lambda)^2$ |
| ζ_{tZu} | 7.484 | $(\zeta_{tZu})^2$ |
| ζ_{tZc} | 1.038 | $(\zeta_{tZc})^2$ |

The top pair cross sections are derived from the SM $t\bar{t}$ cross section, calculated with `MadGraph5_aMC@NLO` at NLO ($\sigma_{t\bar{t}} = 6.741 \cdot 10^2$ pb), and considering the decay $t\bar{t} \rightarrow (bW^\pm)(X_{qt})$. The branching ratio $\mathcal{B}(t \rightarrow bW^\pm)$ is assumed to be equal to one and the FCNC branching ratio is calculated as

$$\mathcal{B}(t \rightarrow qX) = \frac{\Gamma_{t \rightarrow qX}}{\Gamma_t^{\text{SM}} + \Gamma_t^{\text{FCNC}}} \approx \frac{\Gamma_{t \rightarrow qX}}{\Gamma_t^{\text{SM}}}, \quad (3.1)$$

NOTE: 665
these partial widths are at LO, how does this relate to NLO that is used? Or is there no difference?

where $\Gamma_{t \rightarrow qX}$ is given in Table 3.1, and the assumption $\Gamma_t^{\text{FCNC}} \ll \Gamma_t^{\text{SM}}$ is made. In Table 3.3 the resulting NLO cross sections for the top-Z FCNC interactions are given.

Table 3.3: Next to leading order top pair cross section for the top-Z FCNC interactions with a full leptonic decay.

| Anomalous coupling | Process | Cross section (pb) |
|------------------------|--|---|
| κ_{tZu}/Λ | $t\bar{t} \rightarrow (b\ell^+\nu)(\bar{u}\ell^+\ell^-)$ | $1.728 \cdot 10^6 (\kappa_{tZu}/\Lambda)^2$ |
| | $t\bar{t} \rightarrow (\bar{b}\ell^-\nu)(u\ell^+\ell^-)$ | $1.728 \cdot 10^6 (\kappa_{tZu}/\Lambda)^2$ |
| κ_{tZc}/Λ | $t\bar{t} \rightarrow (b\ell^+\nu)(\bar{c}\ell^+\ell^-)$ | $1.728 \cdot 10^6 (\kappa_{tZc}/\Lambda)^2$ |
| | $t\bar{t} \rightarrow (\bar{b}\ell^-\nu)(c\ell^+\ell^-)$ | $1.728 \cdot 10^6 (\kappa_{tZc}/\Lambda)^2$ |
| ζ_{tZu} | $t\bar{t} \rightarrow (b\ell^+\nu)(\bar{u}\ell^+\ell^-)$ | $1.728 \cdot 10^6 (\zeta_{tZu})^2$ |
| | $t\bar{t} \rightarrow (\bar{b}\ell^-\nu)(u\ell^+\ell^-)$ | $1.728 \cdot 10^6 (\zeta_{tZu})^2$ |
| ζ_{tZc} | $t\bar{t} \rightarrow (b\ell^+\nu)(\bar{c}\ell^+\ell^-)$ | $1.728 \cdot 10^6 (\zeta_{tZc})^2$ |
| | $t\bar{t} \rightarrow (\bar{b}\ell^-\nu)(c\ell^+\ell^-)$ | $1.728 \cdot 10^6 (\zeta_{tZc})^2$ |

667 **3.1.4 Generating background events**

668 **3.2 Multivariate analysis techniques: Boosted Decision Trees**

669 **3.3 Template-based fitting**

Bibliography

- 671 [1] MICHAEL E PESKIN and DANIEL V SCHROEDER: **An introduction to quantum field**
 672 **theory; 1995 ed.** Includes exercises. Boulder, CO: Westview, 1995. URL: <https://cds.cern.ch/record/257493> (see pp. 1, 5).
- 674 [2] NADIA ROBOTTI: **The discovery of the electron: I.** In: *European Journal of Physics*, **18**:3
 675 (1997), p. 133. URL: <http://stacks.iop.org/0143-0807/18/i=3/a=002> (see p. 1).
- 676 [3] C. PATRIGNANI et al.: **Review of Particle Physics.** In: *Chin. Phys.*, **C40**:10 (2016),
 677 p. 100001. DOI: [10.1088/1674-1137/40/10/100001](https://doi.org/10.1088/1674-1137/40/10/100001) (see pp. 2–3, 6).
- 678 [4] S. ABACHI et al.: **Observation of the top quark.** In: *Phys. Rev. Lett.*, **74**: (1995),
 679 pp. 2632–2637. DOI: [10.1103/PhysRevLett.74.2632](https://doi.org/10.1103/PhysRevLett.74.2632). arXiv: [hep-ex/9503003](https://arxiv.org/abs/hep-ex/9503003) [hep-ex]
 680 (see p. 2).
- 681 [5] F. ABE et al.: **Observation of top quark production in $\bar{p}p$ collisions.** In: *Phys. Rev. Lett.*, **74**: (1995),
 682 pp. 2626–2631. DOI: [10.1103/PhysRevLett.74.2626](https://doi.org/10.1103/PhysRevLett.74.2626). arXiv: [hep-ex/9503002](https://arxiv.org/abs/hep-ex/9503002) [hep-ex] (see p. 2).
- 684 [6] SERGUEI CHATRHYAN et al.: **Observation of a new boson at a mass of 125 GeV with**
 685 **the CMS experiment at the LHC.** In: *Phys. Lett.*, **B716**: (2012), pp. 30–61. DOI:
 686 [10.1016/j.physletb.2012.08.021](https://doi.org/10.1016/j.physletb.2012.08.021). arXiv: [1207.7235](https://arxiv.org/abs/1207.7235) [hep-ex] (see pp. 2, 13).
- 687 [7] GEORGES AAD et al.: **Observation of a new particle in the search for the Standard**
 688 **Model Higgs boson with the ATLAS detector at the LHC.** In: *Phys. Lett.*, **B716**:
 689 (2012), pp. 1–29. DOI: [10.1016/j.physletb.2012.08.020](https://doi.org/10.1016/j.physletb.2012.08.020). arXiv: [1207.7214](https://arxiv.org/abs/1207.7214) [hep-ex]
 690 (see pp. 2, 13).
- 691 [8] NICOLA CABIBBO: **Unitary Symmetry and Leptonic Decays.** In: *Phys. Rev. Lett.*, **10**:
 692 (12 June 1963), pp. 531–533. DOI: [10.1103/PhysRevLett.10.531](https://doi.org/10.1103/PhysRevLett.10.531) (see p. 5).
- 693 [9] S. L. GLASHOW, J. ILIOPOULOS, and L. MAIANI: **Weak Interactions with Lepton-Hadron**
 694 **Symmetry.** In: *Phys. Rev. D*, **2**: (7 Oct. 1970), pp. 1285–1292. DOI: [10.1103/PhysRevD.2.1285](https://doi.org/10.1103/PhysRevD.2.1285) (see p. 5).
- 696 [10] B.J. BJØRKEN and S.L. GLASHOW: **Elementary particles and SU(4).** In: *Physics Letters*,
 697 **11**:3 (1964), pp. 255–257. DOI: [https://doi.org/10.1016/0031-9163\(64\)90433-0](https://doi.org/10.1016/0031-9163(64)90433-0) (see
 698 p. 5).

- [11] LUCIANO MAIANI: **The GIM Mechanism: origin, predictions and recent uses.** In: *Proceedings, 48th Rencontres de Moriond on Electroweak Interactions and Unified Theories: La Thuile, Italy, March 2-9, 2013.* 2013, pp. 3–16. arXiv: 1303.6154 [hep-ph]. URL: <https://inspirehep.net/record/1225307/files/arXiv:1303.6154.pdf> (see p. 5).
- [12] PATRICK KOPPENBURG and SEBASTIEN DESCOTES-GENON: **The CKM Parameters.** In: (2017). arXiv: 1702.08834 [hep-ex] (see p. 6).
- [13] J. A. AGUILAR-SAAVEDRA: **Top flavor-changing neutral interactions: Theoretical expectations and experimental detection.** In: *Acta Phys. Polon., B35:* (2004), pp. 2695–2710. arXiv: hep-ph/0409342 [hep-ph] (see pp. 6, 8–9).
- [14] YORIKIYO NAGASHIMA: **Beyond the standard model of elementary particle physics.** Weinheim, Germany: Wiley-VCH Verlag, 2014. URL: <http://www-spires.fnal.gov/spires/find/books/www?cl=QC793.2.N34::2014> (see p. 6).
- [15] Y. FUKUDA et al.: **Evidence for oscillation of atmospheric neutrinos.** In: *Phys. Rev. Lett., 81:* (1998), pp. 1562–1567. DOI: 10.1103/PhysRevLett.81.1562. arXiv: hep-ex/9807003 [hep-ex] (see p. 7).
- [16] Y. ABE et al.: **Indication of Reactor $\bar{\nu}_e$ Disappearance in the Double Chooz Experiment.** In: *Phys. Rev. Lett., 108:* (13 Mar. 2012), p. 131801. DOI: 10.1103/PhysRevLett.108.131801 (see p. 7).
- [17] P. A. R. ADE et al.: **Planck 2015 results. XIII. Cosmological parameters.** In: *Astron. Astrophys., 594:* (2016), A13. DOI: 10.1051/0004-6361/201525830. arXiv: 1502.01589 [astro-ph.CO] (see p. 7).
- [18] P. J. E. PEEBLES and BHARAT RATRA: **The Cosmological constant and dark energy.** In: *Rev. Mod. Phys., 75:* (2003), pp. 559–606. DOI: 10.1103/RevModPhys.75.559. arXiv: astro-ph/0207347 [astro-ph] (see p. 7).
- [19] A. D. SAKHAROV: **Violation of CP Invariance, c Asymmetry, and Baryon Asymmetry of the Universe.** In: *Pisma Zh. Eksp. Teor. Fiz., 5:* (1967). [Usp. Fiz. Nauk 161, 61 (1991)], pp. 32–35. DOI: 10.1070/PU1991v034n05ABEH002497 (see p. 7).
- [20] GUSTAVO BURDMAN: **New solutions to the hierarchy problem.** In: *Braz. J. Phys., 37:* (2007), pp. 506–513. DOI: 10.1590/S0100-97332007000400006. arXiv: hep-ph/0703194 [hep-ph] (see p. 7).
- [21] T. ET AL. AALTONEN: **Search for the Flavor-Changing Neutral-Current Decay $t \rightarrow Zq$ in $p\bar{p}$ Collisions at $\sqrt{s} = 1.96$ TeV.** In: *Phys. Rev. Lett., 101:* (19 Nov. 2008), p. 192002. DOI: 10.1103/PhysRevLett.101.192002 (see p. 8).
- [22] VICTOR MUKHAMEDOVICH ABAZOV et al.: **Search for flavour changing neutral currents via quark-gluon couplings in single top quark production using 2.3 fb^{-1} of $p\bar{p}$ collisions.** In: *Phys. Lett., B693:* (2010), pp. 81–87. DOI: 10.1016/j.physletb.2010.08.011. arXiv: 1006.3575 [hep-ex] (see p. 8).
- [23] GEORGES AAD et al.: **Search for flavour-changing neutral current top-quark decays to qZ in pp collision data collected with the ATLAS detector at $\sqrt{s} = 8$ TeV.** In: *Eur. Phys. J., C76:1* (2016), p. 12. DOI: 10.1140/epjc/s10052-015-3851-5. arXiv: 1508.05796 [hep-ex] (see p. 8).

- 740 [24] GEORGES AAD et al.: **Search for single top-quark production via flavour-changing**
 741 **neutral currents at 8 TeV with the ATLAS detector.** In: *Eur. Phys. J.*, **C76**:2 (2016),
 742 p. 55. doi: [10.1140/epjc/s10052-016-3876-4](https://doi.org/10.1140/epjc/s10052-016-3876-4). arXiv: [1509.00294 \[hep-ex\]](https://arxiv.org/abs/1509.00294) (see pp. 8,
 743 11).
- 744 [25] GEORGES AAD et al.: **Search for flavour-changing neutral current top quark decays**
 745 $t \rightarrow Hq$ **in pp collisions at $\sqrt{s} = 8$ TeV with the ATLAS detector.** In: *JHEP*, **12**:
 746 (2015), p. 061. doi: [10.1007/JHEP12\(2015\)061](https://doi.org/10.1007/JHEP12(2015)061). arXiv: [1509.06047 \[hep-ex\]](https://arxiv.org/abs/1509.06047) (see p. 8).
- 747 [26] MORAD AABOUD et al.: **Search for top quark decays $t \rightarrow qH$, with $H \rightarrow \gamma\gamma$, in $\sqrt{s} = 13$**
 748 **TeV pp collisions using the ATLAS detector.** In: (2017). arXiv: [1707.01404 \[hep-ex\]](https://arxiv.org/abs/1707.01404)
 749 (see pp. 8, 11).
- 750 [27] ALBERT M SIRUNYAN et al.: **Search for associated production of a Z boson with a**
 751 **single top quark and for tZ flavour-changing interactions in pp collisions at $\sqrt{s} =$**
 752 **8 TeV.** In: (2017). arXiv: [1702.01404 \[hep-ex\]](https://arxiv.org/abs/1702.01404) (see pp. 8, 11).
- 753 [28] SERGUEI CHATRCHYAN et al.: **Search for Flavor-Changing Neutral Currents in Top-**
 754 **Quark Decays $t \rightarrow Zq$ in pp Collisions at $\sqrt{s} = 8$ TeV.** In: *Phys. Rev. Lett.*, **112**:17
 755 (2014), p. 171802. doi: [10.1103/PhysRevLett.112.171802](https://doi.org/10.1103/PhysRevLett.112.171802). arXiv: [1312.4194 \[hep-ex\]](https://arxiv.org/abs/1312.4194)
 756 (see p. 8).
- 757 [29] VARDAN KHACHATRYAN et al.: **Search for anomalous single top quark production in**
 758 **association with a photon in pp collisions at $\sqrt{s} = 8$ TeV.** In: *JHEP*, **04**: (2016),
 759 p. 035. doi: [10.1007/JHEP04\(2016\)035](https://doi.org/10.1007/JHEP04(2016)035). arXiv: [1511.03951 \[hep-ex\]](https://arxiv.org/abs/1511.03951) (see pp. 8, 11).
- 760 [30] VARDAN KHACHATRYAN et al.: **Search for top quark decays via Higgs-boson-mediated**
 761 **flavor-changing neutral currents in pp collisions at $\sqrt{s} = 8$ TeV.** In: *JHEP*, **02**:
 762 (2017), p. 079. doi: [10.1007/JHEP02\(2017\)079](https://doi.org/10.1007/JHEP02(2017)079). arXiv: [1610.04857 \[hep-ex\]](https://arxiv.org/abs/1610.04857) (see p. 8).
- 763 [31] **Search for the flavor-changing interactions of the top quark with the Higgs boson**
 764 **in $H \rightarrow b\bar{b}$ channel at $\sqrt{s} = 13$ TeV.** Tech. rep. CMS-PAS-TOP-17-003. Geneva: CERN,
 765 2017. URL: <https://cds.cern.ch/record/2284743> (see p. 8).
- 766 [32] J. A. AGUILAR-SAAVEDRA: **A Minimal set of top anomalous couplings.** In: *Nucl. Phys.*,
 767 **B812**: (2009), pp. 181–204. doi: [10.1016/j.nuclphysb.2008.12.012](https://doi.org/10.1016/j.nuclphysb.2008.12.012). arXiv: [0811.3842 \[hep-ph\]](https://arxiv.org/abs/0811.3842) (see p. 9).
- 769 [33] J. A. AGUILAR-SAAVEDRA: **A Minimal set of top-Higgs anomalous couplings.** In: *Nucl.*
 770 *Phys.*, **B821**: (2009), pp. 215–227. doi: [10.1016/j.nuclphysb.2009.06.022](https://doi.org/10.1016/j.nuclphysb.2009.06.022). arXiv:
 771 [0904.2387 \[hep-ph\]](https://arxiv.org/abs/0904.2387) (see p. 9).
- 772 [34] M. BENEKE et al.: **Top quark physics.** In: *1999 CERN Workshop on standard model*
 773 *physics (and more) at the LHC, CERN, Geneva, Switzerland, 25-26 May: Proceedings.* 2000,
 774 pp. 419–529. arXiv: [hep-ph/0003033 \[hep-ph\]](https://arxiv.org/abs/hep-ph/0003033). URL: <http://weblib.cern.ch/abstract?CERN-TH-2000-100> (see p. 9).
- 776 [35] JUN GAO, CHONG SHENG LI, and HUA XING ZHU: **Top Quark Decay at Next-to-Next-to**
 777 **Leading Order in QCD.** In: *Phys. Rev. Lett.*, **110**:4 (2013), p. 042001. doi: [10.1103/PhysRevLett.110.042001](https://doi.org/10.1103/PhysRevLett.110.042001). arXiv: [1210.2808 \[hep-ph\]](https://arxiv.org/abs/1210.2808) (see p. 10).
- 779 [36] STEPHEN MYERS: **The LEP Collider, from design to approval and commissioning.**
 780 John Adams' Lecture. Delivered at CERN, 26 Nov 1990. Geneva: CERN, 1991. URL:
 781 [http://cds.cern.ch/record/226776](https://cds.cern.ch/record/226776) (see p. 13).

- [37] STEPHEN HOLMES, RONALD S MOORE, and VLADIMIR SHILTSEV: **Overview of the Tevatron collider complex: goals, operations and performance.** In: *Journal of Instrumentation*, 6:08 (2011), T08001. URL: <http://stacks.iop.org/1748-0221/6/i=08/a=T08001> (see p. 13).
- [38] R. BARATE et al.: **Search for the standard model Higgs boson at LEP.** In: *Phys. Lett.*, B565: (2003), pp. 61–75. DOI: [10.1016/S0370-2693\(03\)00614-2](https://doi.org/10.1016/S0370-2693(03)00614-2). arXiv: [hep-ex/0306033 \[hep-ex\]](https://arxiv.org/abs/hep-ex/0306033) (see p. 13).
- [39] KENNETH HERNER: **Higgs Boson Studies at the Tevatron.** In: *Nucl. Part. Phys. Proc.*, 273-275: (2016), pp. 852–856. DOI: [10.1016/j.nuclphysbps.2015.09.131](https://doi.org/10.1016/j.nuclphysbps.2015.09.131) (see p. 13).
- [40] ABDELHAK DJOUADI: **The Anatomy of electro-weak symmetry breaking. I: The Higgs boson in the standard model.** In: *Phys. Rept.*, 457: (2008), pp. 1–216. DOI: [10.1016/j.physrep.2007.10.004](https://doi.org/10.1016/j.physrep.2007.10.004). arXiv: [hep-ph/0503172 \[hep-ph\]](https://arxiv.org/abs/hep-ph/0503172) (see p. 13).
- [41] LYNDON EVANS and PHILIP BRYANT: **LHC Machine.** In: *Journal of Instrumentation*, 3:08 (2008), S08001. URL: <http://stacks.iop.org/1748-0221/3/i=08/a=S08001> (see p. 13).
- [42] THOMAS SVEN PETTERSSON and P LEFÈVRE: **The Large Hadron Collider: conceptual design.** Tech. rep. CERN-AC-95-05-LHC. Oct. 1995, p. 20 and 22. URL: <https://cds.cern.ch/record/291782> (see p. 13).
- [43] JORG WENNINGER and EZIO TODESCO: **Large Hadron Collider momentum calibration and accuracy.** Tech. rep. CERN-ACC-2017-0007. Geneva: CERN, Feb. 2017. URL: <https://cds.cern.ch/record/2254678> (see p. 14).
- [44] CINZIA DE MELIS: **The CERN accelerator complex. Complexe des accélérateurs du CERN.** In: (July 2016). General Photo. URL: <https://cds.cern.ch/record/2197559> (see p. 14).
- [45] G. AAD et al.: **The ATLAS Experiment at the CERN Large Hadron Collider.** In: *JINST*, 3: (2008), S08003. DOI: [10.1088/1748-0221/3/08/S08003](https://doi.org/10.1088/1748-0221/3/08/S08003) (see p. 14).
- [46] S. CHATRCHYAN et al.: **The CMS Experiment at the CERN LHC.** In: *JINST*, 3: (2008), S08004. DOI: [10.1088/1748-0221/3/08/S08004](https://doi.org/10.1088/1748-0221/3/08/S08004) (see pp. 14, 23).
- [47] K. AAMODT et al.: **The ALICE experiment at the CERN LHC.** In: *JINST*, 3: (2008), S08002. DOI: [10.1088/1748-0221/3/08/S08002](https://doi.org/10.1088/1748-0221/3/08/S08002) (see p. 14).
- [48] A. AUGUSTO ALVES JR. et al.: **The LHCb Detector at the LHC.** In: *JINST*, 3: (2008), S08005. DOI: [10.1088/1748-0221/3/08/S08005](https://doi.org/10.1088/1748-0221/3/08/S08005) (see p. 14).
- [49] M. BONGI et al.: **Astroparticle physics at LHC: The LHCf experiment ready for data taking.** In: *Nucl. Instrum. Meth.*, A612: (2010), pp. 451–454. DOI: [10.1016/j.nima.2009.08.039](https://doi.org/10.1016/j.nima.2009.08.039) (see p. 14).
- [50] G. ANELLI et al.: **The TOTEM experiment at the CERN Large Hadron Collider.** In: *JINST*, 3: (2008), S08007. DOI: [10.1088/1748-0221/3/08/S08007](https://doi.org/10.1088/1748-0221/3/08/S08007) (see p. 14).
- [51] B. ACHARYA et al.: **The Physics Programme Of The MoEDAL Experiment At The LHC.** In: *Int. J. Mod. Phys.*, A29: (2014), p. 1430050. DOI: [10.1142/S0217751X14300506](https://doi.org/10.1142/S0217751X14300506). arXiv: [1405.7662 \[hep-ph\]](https://arxiv.org/abs/1405.7662) (see p. 15).
- [52] BY JAMES GILLIES: **Luminosity? Why don't we just say collision rate?** In: (Mar. 2011). URL: <https://cds.cern.ch/record/1997001> (see p. 15).

- 823 [53] BY HARRIET JARLETT and HARRIET KIM JARLETT: **LHC pushes limits of performance.**
 824 In: (Aug. 2016). URL: <http://cds.cern.ch/record/2212301> (see p. 15).
- 825 [54] OLIVER SIM BRÜNING, PAUL COLLIER, P LEBRUN, et al.: **LHC Design Report.** CERN Yellow
 826 Reports: Monographs. Geneva: CERN, 2004. URL: <https://cds.cern.ch/record/782076>
 827 (see p. 15).
- 828 [55] JEAN-LUC CARON: **Cross section of LHC dipole.. Dipole LHC: coupe transversale.**
 829 AC Collection. Legacy of AC. Pictures from 1992 to 2002. May 1998. URL: <https://cds.cern.ch/record/841539> (see p. 16).
- 831 [56] **Technical proposal.** LHC Tech. Proposal. Cover title : CMS, the Compact Muon Solenoid
 832 : technical proposal. Geneva: CERN, 1994. URL: <https://cds.cern.ch/record/290969>
 833 (see p. 17).
- 834 [57] G. L. BAYATIAN et al.: **CMS physics: Technical design report.** In: (2006) (see pp. 17,
 835 25).
- 836 [58] G L BAYATIAN, S CHATRCHYAN, G HMAYAKYAN, et al.: **CMS Physics: Technical Design**
 837 **Report Volume 1: Detector Performance and Software.** Technical Design Report CMS.
 838 There is an error on cover due to a technical problem for some items. Geneva: CERN,
 839 2006. URL: <https://cds.cern.ch/record/922757> (see pp. 17, 21, 26).
- 840 [59] BY CIAN O'LUANAIGH: **LHC progresses towards higher intensities.** In: (Aug. 2015).
 841 URL: <http://cds.cern.ch/record/2051986> (see p. 17).
- 842 [60] CMS COLLABORATION: **Detector Drawings.** CMS Collection. Mar. 2012. URL: <https://cds.cern.ch/record/1433717> (see p. 18).
- 844 [61] BY CORINNE PRALAVORIO and CORINNE PRALAVORIO: **Major work to ready the LHC**
 845 **experiments for Run 2.** In: (May 2015). URL: <http://cds.cern.ch/record/2024977>
 846 (see pp. 17, 26).
- 847 [62] S CHATRCHYAN, V KHACHATRYAN, A M SIRUNYAN, et al.: **Performance of the CMS Drift**
 848 **Tube Chambers with Cosmic Rays.** In: *J. Instrum.*, 5:arXiv:0911.4855. CMS-CFT-
 849 09-012 (Nov. 2009), T03015 . 47 p. URL: <http://cds.cern.ch/record/1223944> (see
 850 pp. 19–20).
- 851 [63] LUIGI GUIDUCCI: **CMS muon system towards LHC Run 2 and beyond.** Tech. rep. CMS-
 852 CR-2014-333. Geneva: CERN, Oct. 2014. URL: <https://cds.cern.ch/record/1966038>
 853 (see p. 20).
- 854 [64] CARLO BATTILANA: **The CMS muon system status and upgrades for LHC run-2 and**
 855 **performance of muon reconstruction with 13 TeV data.** Tech. rep. CMS-CR-2016-
 856 437. Geneva: CERN, Dec. 2016. URL: <http://cds.cern.ch/record/2239185> (see
 857 p. 20).
- 858 [65] SERGUEI CHATRCHYAN et al.: **Performance of CMS muon reconstruction in pp col-**
 859 **lision events at $\sqrt{s} = 7$ TeV.** In: *JINST*, 7: (2012), P10002. DOI: [10.1088/1748-0221/7/10/P10002](https://doi.org/10.1088/1748-0221/7/10/P10002). arXiv: [1206.4071 \[physics.ins-det\]](https://arxiv.org/abs/1206.4071) (see p. 21).
- 861 [66] R. FRÜHWIRTH: **Application of Kalman filtering to track and vertex fitting.** In: *Nu-*
 862 *clear Instruments and Methods in Physics Research Section A: Accelerators, Spectrom-*
 863 *eters, Detectors and Associated Equipment*, 262:2 (1987), pp. 444–450. DOI: [http://dx.doi.org/10.1016/0168-9002\(87\)90887-4](https://doi.org/10.1016/0168-9002(87)90887-4) (see pp. 21, 27).

- 865 [67] PIERRE BILLOIR: **Progressive track recognition with a Kalman like fitting procedure.**
 866 In: *Comput. Phys. Commun.*, **57**: (1989), pp. 390–394. doi: [10.1016/0010-4655\(89\)
 867 90249-X](https://doi.org/10.1016/0010-4655(89)90249-X) (see pp. 21, 27).
- 868 [68] EMRAH TIRAS, BURAK BILKI, and YASAR ONEL: **Commissioning of CMS Forward Hadron
 869 Calorimeters with Upgraded Multi-anode PMTs and μ TCA Readout.** In: (2016).
 870 arXiv: [1611.05232 \[physics.ins-det\]](https://arxiv.org/abs/1611.05232) (see p. 22).
- 871 [69] L. BRIANZA: **Precision crystal calorimetry in LHC Run II with the CMS ECAL.** In:
 872 *Journal of Instrumentation*, **12**:01 (2017), p. C01069. URL: [http://stacks.iop.org/1748-
 873 0221/12/i=01/a=C01069](http://stacks.iop.org/1748-0221/12/i=01/a=C01069) (see p. 24).
- 874 [70] SERGUEI CHATRCHYAN et al.: **Energy Calibration and Resolution of the CMS Elec-
 875 tromagnetic Calorimeter in pp Collisions at $\sqrt{s} = 7$ TeV.** In: *JINST*, **8**: (2013).
 876 [*JINST*8,9009(2013)], P09009. doi: [10.1088/1748-0221/8/09/P09009](https://doi.org/10.1088/1748-0221/8/09/P09009). arXiv: [1306.2016
 877 \[hep-ex\]](https://arxiv.org/abs/1306.2016) (see p. 24).
- 878 [71] SERGUEI CHATRCHYAN, VARDAN KHACHATRYAN, ALBERT M SIRUNYAN, et al.: **Description
 879 and performance of track and primary-vertex reconstruction with the CMS tracker.**
 880 In: *J. Instrum.*, **9**:arXiv:1405.6569. CERN-PH-EP-2014-070. CMS-TRK-11-001 (May
 881 2014). Comments: Replaced with published version. Added journal reference and DOI,
 882 P10009. 80 p. URL: <http://cds.cern.ch/record/1704291> (see pp. 24, 27).
- 883 [72] BY CHRISTINE SUTTON: **Chronicles of CMS: the saga of LS1.** In: (May 2015). URL:
 884 <http://cds.cern.ch/record/2024986> (see p. 26).
- 885 [73] **A beautiful barrel for CMS.** In: (Mar. 2014). URL: [http://cds.cern.ch/record/
 886 1998635](http://cds.cern.ch/record/1998635) (see p. 26).
- 887 [74] **Cool running for CMS tracker.** In: (Mar. 2014). URL: [http://cds.cern.ch/record/
 888 1998606](http://cds.cern.ch/record/1998606) (see p. 26).
- 889 [75] K. ROSE: **Deterministic annealing for clustering, compression, classification, re-
 890 gression, and related optimization problems.** In: *Proceedings of the IEEE*, **86**:11 (Nov.
 891 1998), pp. 2210–2239. doi: [10.1109/5.726788](https://doi.org/10.1109/5.726788) (see p. 27).
- 892 [76] WOLFGANG WALTENBERGER: **Adaptive Vertex Reconstruction.** Tech. rep. CMS-NOTE-
 893 2008-033. Geneva: CERN, July 2008. URL: <https://cds.cern.ch/record/1166320> (see
 894 p. 27).
- 895 [77] L. CADAMURO: **The CMS Level-1 trigger system for LHC Run II.** In: *Journal of Instru-
 896 mentation*, **12**:03 (2017), p. C03021. URL: [http://stacks.iop.org/1748-0221/12/i=03/
 897 a=C03021](http://stacks.iop.org/1748-0221/12/i=03/a=C03021) (see p. 28).
- 898 [78] VARDAN KHACHATRYAN et al.: **The CMS trigger system.** In: *JINST*, **12**:01 (2017),
 899 P01020. doi: [10.1088/1748-0221/12/01/P01020](https://doi.org/10.1088/1748-0221/12/01/P01020). arXiv: [1609.02366 \[physics.ins-det\]](https://arxiv.org/abs/1609.02366)
 900 (see p. 28).
- 901 [79] CLAUDIO GRANDI, DAVID STICKLAND, LUCAS TAYLOR, ACHILLE PETRILLI, and ALAIN HERVÉ:
 902 **CMS Computing Model: The "CMS Computing Model RTAG".** Tech. rep. CMS-NOTE-
 903 2004-031. CERN-LHCC-2004-035. LHCC-G-083. Geneva: CERN, Dec. 2004. URL:
 904 <http://cds.cern.ch/record/814248> (see p. 28).

- 905 [80] CHRISTOPH ECK, J KNOBLOCH, LESLIE ROBERTSON, et al.: **LHC computing Grid: Technical Design Report. Version 1.06 (20 Jun 2005)**. Technical Design Report LCG. Geneva: CERN, 2005. URL: <https://cds.cern.ch/record/840543> (see p. 28).
- 906
- 907
- 908 [81] S BANERJEE: **CMS Simulation Software**. In: *Journal of Physics: Conference Series*, **396**:2 (2012), p. 022003. URL: <http://stacks.iop.org/1742-6596/396/i=2/a=022003> (see p. 31).
- 909
- 910
- 911 [82] M HILDRETH, VN IVANCHENKO, D J LANGE, and M J KORTELAINEN: **CMS Full Simulation for Run-2**. In: *Journal of Physics: Conference Series*, **664**:7 (2015), p. 072022. URL: <http://stacks.iop.org/1742-6596/664/i=7/a=072022> (see p. 31).
- 912
- 913
- 914 [83] S. AGOSTINELLI, J. ALLISON, K. AMAKO, et al.: **Geant4—a simulation toolkit**. In: *Nuclear Instruments and Methods in Physics Research Section A: Accelerators, Spectrometers, Detectors and Associated Equipment*, **506**:3 (2003), pp. 250–303. DOI: [https://doi.org/10.1016/S0168-9002\(03\)01368-8](https://doi.org/10.1016/S0168-9002(03)01368-8) (see p. 31).
- 915
- 916
- 917
- 918 [84] MICHAEL H. SEYMOUR and MARILYN MARX: **Monte Carlo Event Generators**. In: *Proceedings, 69th Scottish Universities Summer School in Physics : LHC Phenomenology (SUSSP69): St.Andrews, Scotland, August 19-September 1, 2012*. 2013, pp. 287–319. DOI: 10.1007/978-3-319-05362-2_8. arXiv: <1304.6677> [hep-ph] (see p. 31).
- 919
- 920
- 921
- 922 [85] TORBJORN SJOSTRAND: **Monte Carlo Tools**. In: *Proceedings, 65th Scottish Universities Summer School in Physics: LHC Physics (SUSSP65): St. Andrews, UK, August 16-29, 2009*. 2009, pp. 309–339. DOI: <10.1201/b11865-14>. arXiv: <0911.5286> [hep-ph] (see p. 31).
- 923
- 924
- 925 [86] STEFAN HÖCHE: **Introduction to parton-shower event generators**. In: *Proceedings, Theoretical Advanced Study Institute in Elementary Particle Physics: Journeys Through the Precision Frontier: Amplitudes for Colliders (TASI 2014): Boulder, Colorado, June 2-27, 2014*. 2015, pp. 235–295. DOI: 10.1142/9789814678766_0005. arXiv: <1411.4085> [hep-ph] (see pp. 31–32).
- 926
- 927
- 928
- 929
- 930 [87] RINGAILE PLACAKYTE: **Parton Distribution Functions**. In: *Proceedings, 31st International Conference on Physics in collisions (PIC 2011): Vancouver, Canada, August 28-September 1, 2011*. 2011. arXiv: <1111.5452> [hep-ph]. URL: <https://inspirehep.net/record/954990/files/arXiv:1111.5452.pdf> (see p. 31).
- 931
- 932
- 933